

## **Section 1**

Assimilation of atmospheric and land  
observations.

Data impact and sensitivity studies.

Methodological advances.



# Real-Time Analysis of Atmospheric Thermodynamic Conditions based on 1DVAR Method using Ground-Based Microwave Radiometer Data

Kentaro Araki<sup>1</sup>,

Masataka Murakami<sup>2,1</sup>, Akihiro Hashimoto<sup>1</sup>, and Takuya Tajiri<sup>1</sup>

*1: Meteorological Research Institute, Tsukuba, Ibaraki, Japan*

*2: Institute for Space-Earth Environmental Research, Nagoya University, Nagoya, Aichi, Japan*

e-mail: araki@mri-jma.go.jp

## 1. Introduction

Forecasts of convective clouds in summer seasons remain challenging, because there is uncertainty in the numerical model reproducibility of low-level atmospheric thermodynamic structures. Recently, a ground-based microwave radiometer (MWR) data has been used for estimating accurate thermodynamic profiles in the low-level troposphere through a one dimensional variational (1DVAR) technique using the results of numerical model simulations (Ishimoto, 2015; Araki et al., 2015, 2017). For the diagnosis of convective cloud developments, the 1DVAR analysis using the MWR data with time intervals of a few minutes could be of benefit considering the diurnal variations of atmospheric thermodynamic profiles although radiosonde observation data twice a day has been used in the traditional method. In September 2013, aircraft observation campaign was conducted to investigate the effectiveness of ground-based AgI generators in seeding convective clouds developed around the central mountain region in Japan as part of the joint research project for a renewal of ground-based AgI generator at Ogouchi Dam between the Bureau of Waterwork of the Tokyo Metropolitan Government and the Meteorological Research Institute. To support the aircraft observation, we developed a real-time 1DVAR analysis system for the derivation of accurate atmospheric thermodynamic structures using MWR data and results of high-resolution numerical model simulation.

## 2. Model settings and design of the real-time 1DVAR system

Numerical simulations were performed twice a day by the Japan Meteorological Agency (JMA) Meteorological Research Institute Non-Hydrostatic Model (MRI-NHM) with a horizontal grid spacing of 1 km and a model domain covering the central mountain region during the campaign. Initial and boundary conditions were provided from forecast data of the JMA operational mesoscale model, and the MRI-NHM was run for 12 hours from 00 and 12 UTC. The results of the simulations were used for 1DVAR analysis (Araki et al., 2015) by combining with the observation data from the MWR installed at Ogouchi (35.79°N, 139.05°E, 530 m). We used the ground-based multi-channel MWR (MP-3000A, Radiometrics), which observed the brightness temperature of 21 K-band (22-30 GHz) and 14 V-band (51-59 GHz) microwave channels with a bandwidth of 300 MHz in the zenith direction at time intervals of a few minutes. The results of the simulation were output at 1-hour intervals, and they were interpolated into the time intervals of MWR observations and used for the first guess of the 1DVAR analysis. The 1DVAR retrievals of atmospheric temperature and water vapor profiles were performed every 10 minutes using the latest observation data of the MWR. In this way, we constructed a real-time 1DVAR analysis system for the retrieval of accurate atmospheric thermodynamic structures.

## 3. Real-time 1DVAR analysis of atmospheric thermodynamic conditions

An example of the real-time 1DVAR analysis is shown in Fig. 1. The real-time 1DVAR analysis system output profiles of thermodynamic profiles and a list of thermodynamic indices such as lifted condensation level (LCL), level of free convection (LFC), convective available potential energy (CAPE), Showalter stability index (SSI), and lifted index (LI) at the time of every analysis. The 1DVAR-derived profile data of temperature, water vapor density, and liquid water content was converted into a format processable in the Universal RAwinsonde OBservation program (RAOB; <http://www.raob.com/>), and the data were monitored in the form of time-height cross-section as shown in Fig. 2. During the aircraft observation campaign, the real-time 1DVAR analysis system and monitoring system were used for a flight decision of the convective cloud observation. From the viewpoint of predicting convective cloud developments, it would be effective to monitor the thermodynamic conditions of the atmosphere using this real-time 1DVAR analysis system combined with the kinematic conditions of the atmosphere such as operational surface wind and wind profiler observation.

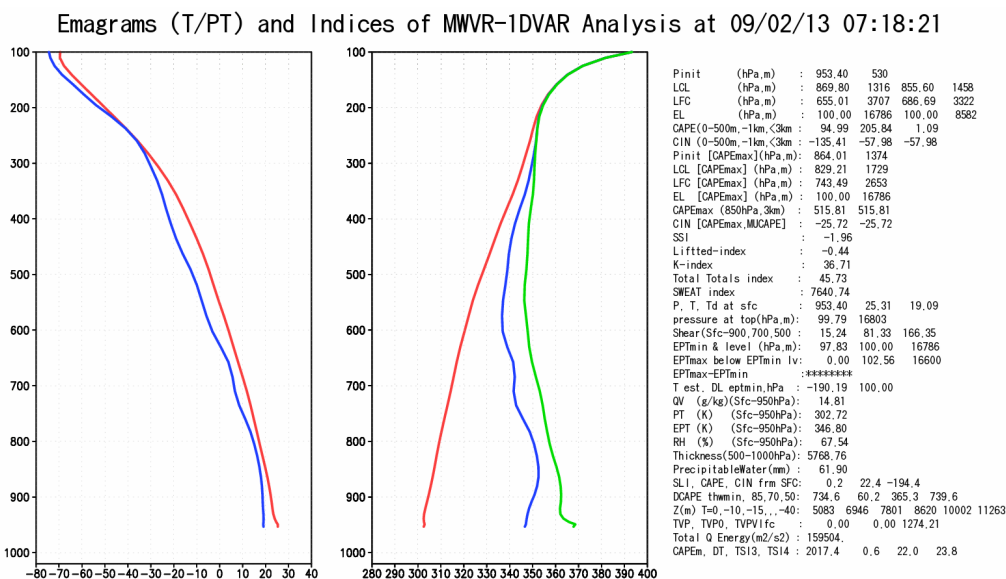


Figure 1. An example of outputs from the real-time 1DVAR analysis system. Red and blue lines in the left panel respectively indicate air temperature and dew point temperature ( $^{\circ}\text{C}$ ) and red, blue, and green lines in the right panel show potential temperature, equivalent potential temperature, and saturated equivalent potential temperature (K), respectively, at 07:18:21 UTC on September 2, 2013.

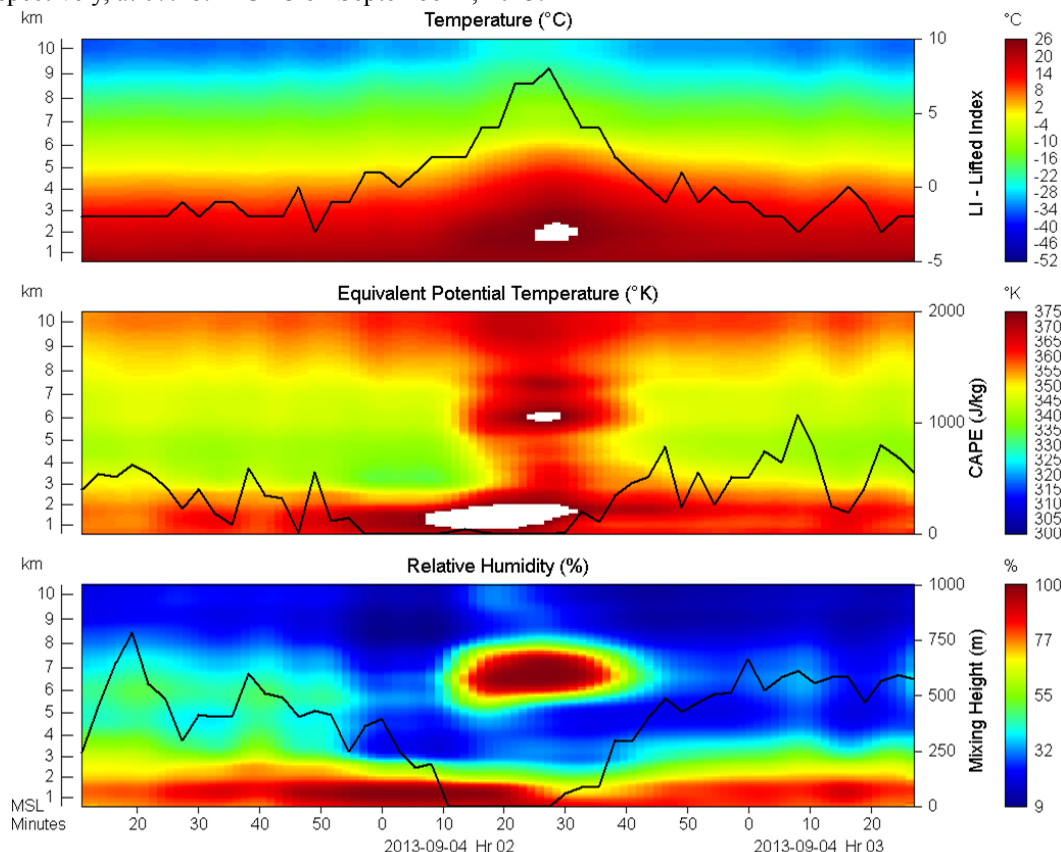


Figure 2. Time-height cross-sections of temperature, equivalent potential temperature, and relative humidity obtained from the real-time 1DVAR analysis system for 02:10:00-03:30:00 UTC on September 4, 2013.

**References:**

Araki, K., M. Murakami, H. Ishimoto, and T. Tajiri, 2015: Ground-based microwave radiometer variational analysis during no-rain and rain conditions. *SOLA*, **11**, 108–112.

Araki, K., M. Murakami, T. Kato, and T. Tajiri, 2017: Analysis of atmospheric environments for convective cloud development around the Central Mountains in Japan during warm seasons using ground-based microwave radiometer data. *Tenki*, **64**, 19–36, (in Japanese with English abstract).

Ishimoto, H., 2015: Analysis of microwave radiometric data using a 1DVAR technique. *Meteor. Res. Notes*, **231**, 259–270, (in Japanese).

# Hourly assimilation including radar, cloud, and surface observations in the NOAA 3km HRRR and 13km RAP models, also with land-atmospheric coupled assimilation

Stan Benjamin, Ming Hu, Curtis Alexander, David Dowell, Haidao Lin, Terra Ladwig, Eric James, Stephen Weygandt, Tatiana Smirnova, Jaymes Kenyon  
 NOAA Earth System Research Laboratory, Boulder, Colorado USA. Stan.Benjamin@noaa.gov

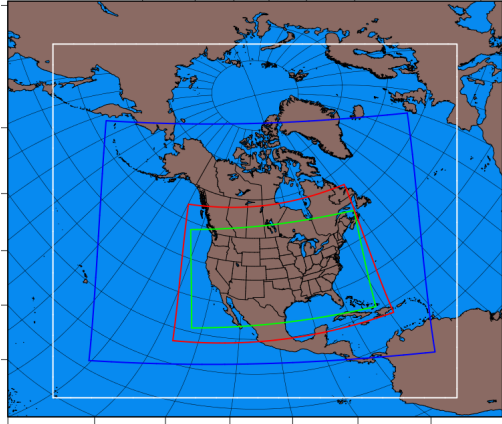


Fig 1. Domains for 3km HRRR model (green) and current RAP (RAPv3, white), Benjamin et al 2016. Also shown for the previous RAP (blue) and previous Rapid Update Cycle models (red).

The 13km Rapid Refresh (**RAP**) analysis and forecast system and 3km High-Resolution Rapid Refresh (**HRRR**) provides *hourly updated* shorter-range forecasts over North America (Fig. 1) for severe weather, aviation/transportation, and other situational awareness decision making. The HRRR runs out to 21 h, with a new data assimilation forecast cycle using latest hourly observations to run new forecasts every hour.

The HRRR and RAP models were recently updated (**HRRRv2/RAPv3**) at NOAA/NCEP in August 2016. An overall description of the RAP/HRRR configuration for model and assimilation details are provided in Benjamin et al 2016 (B16). The RAPv3/HRRRv2 versions featured a largely removed warm/dry bias (Fig. 2, also B16 - section 6) through improved assimilation and model physics.

The HRRR and RAP data assimilation uses a GSI (NOAA's Gridpoint Statistical Interpolation) version enhanced by advanced capabilities for:

1. Hybrid (ensemble/variational) assimilation (B16, Hu et al 2017).

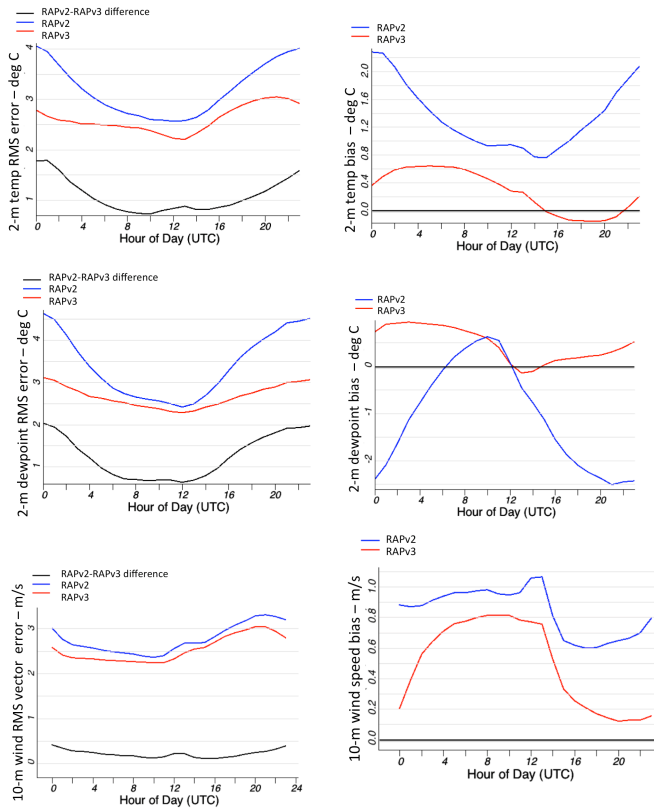


Fig 2. Surface verification over the 4-month period from 1 May – 31 Aug 2015 for 12-h forecasts from RAPv2 and RAPv3 in eastern CONUS region for (left column) RMS error and (right column) bias over period. Both RMS errors and bias are calculated for forecasts versus METAR observations. Statistics in each column are for (top) 2-m temperature, (middle) 2-m dewpoint, and (bottom) 10-m wind. (Benjamin et al 2016, Fig 11)

2. Radar reflectivity assimilation via latent heating. Latent heating is applied via a digital filter initialization in RAP (Reference B16) and directly at 3km at 15min intervals in HRRR (B16).
3. Cloud and precipitation hydrometeor assimilation (B16), using satellite cloud-top and METAR ceiling observations.
4. PBL-based pseudo innovations from surface observations (B16, 2f).
5. Full radiance assimilation in hourly RAP cycle (Lin et al 2017).
6. Soil temperature adjustment via coupled atmospheric-soil assimilation using near-surface atmospheric analysis increments (B16, Smirnova et al 2016).

A more recent observation system (impact) set of experiments for 10 different observation types revealed that short-range RAP forecast skill is most highly dependent on aircraft observations (Fig 3 below, from James and Benjamin 2017). Further improvements in radar, cloud, and surface assimilation are included in the HRRRv3/RAPv4 update currently planned at NCEP in February 2018.

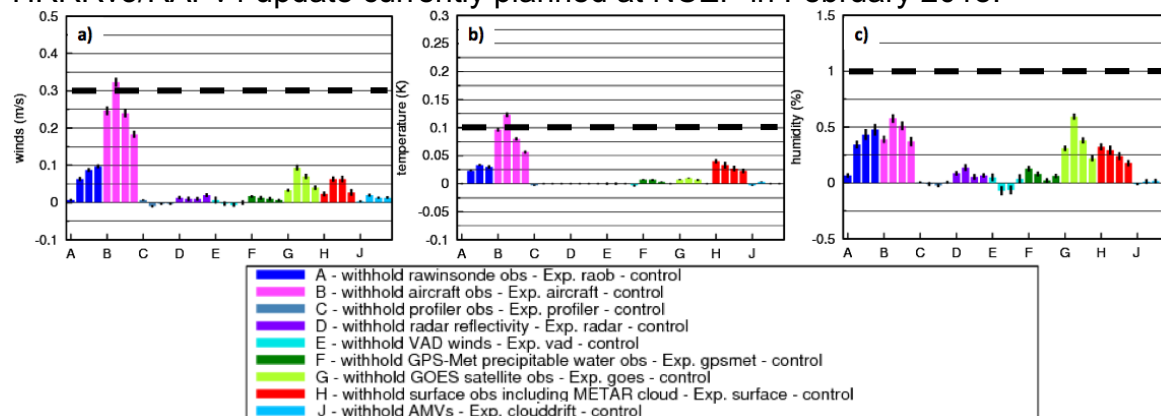


Fig 3. Observation impact results for RAP (increase in 1000-100 hPa 3/6/9/12h forecast vs. raobs when 9 different observation types are withheld. Integrated over 10-day experiments from all three seasons (JB17, Fig. 7) showing results for (a) wind, (b) temperature, and (c) relative humidity. Dashed lines indicate the level of 25% forecast error reduction. Statistical uncertainties are indicated for each experiment by narrow black lines showing  $\pm 1$  standard error from the mean impact.

Benjamin, S. G., S.S. Weygandt, M. Hu, C.A. Alexander, T.G. Smirnova, J.B. Olson, J.M. Brown, E. James, D.C. Dowell, G.A. Grell, H. Lin, S.E. Peckham, T.L. Smith, W.R. Moninger, G.S. Manikin, **2016**, A North American hourly assimilation and model forecast cycle: The Rapid Refresh. *Mon. Wea. Rev.*, **144**, 1669-1694. <http://dx.doi.org/10.1175/MWR-D-15-0242.1>

Hu, M., S.G. Benjamin, T. Ladwig, S.S. Weygandt, **2017**: GSI 3-dimensional ensemble-variational hybrid data assimilation using a global ensemble for the regional Rapid Refresh model. *Mon. Wea. Rev.* Accepted with minor revision.

James, E.P., S.G. Benjamin, **2017**: Observation system experiments with the hourly-updating Rapid Refresh (RAP) Model using GSI hybrid-ensemble/variational (3d) data assimilation. *Mon. Wea. Rev.*, **145**, <http://journals.ametsoc.org/doi/pdf/10.1175/MWR-D-16-0398.1>

Lin, H., S.S. Weygandt, S.G. Benjamin, M. Hu, **2017**: Satellite radiance data assimilation within the hourly updated Rapid Refresh. *Wea. Forecasting*, **32**, 1273-1287.

Smirnova, T.G., J.M. Brown, and S.G. Benjamin, **2016**: Modifications to the Land Surface Model in the transition from the Rapid Update Cycle (RUC) to the WRF-based Rapid Refresh (RAP). *Mon. Wea. Rev.*, **144**, 1851-1865. <http://dx.doi.org/10.1175/MWR-D-15-0198.1>

# Change of variable applied to mass and wind fields for covariance localisation

Loïk BERRE, Etienne ARBOGAST, Benjamin MENETRIER and Gérald DESROZIERS

*Météo-France/CNRS, CNRM, Toulouse, France*

*email : [loik.berre@meteo.fr](mailto:loik.berre@meteo.fr)*

## 1) Formulation of 3DEnVar/4DEnVar based on a common localisation

Data assimilation schemes based on either 3DEnVar or 4DEnVar formulation rely on a representation of background error covariances as a Schur product between a raw ensemble covariance matrix and a localisation matrix, in order to attenuate sampling noise which dominates at long separation distances. For efficiency reasons (e.g. Desroziers et al 2014), such formulations usually employ a common horizontal localisation function (at a given vertical level) for auto-covariances of all variables and also for associated cross-covariances. Moreover, this common horizontal localisation function usually depends on separation distance only, and it is thus isotropic.

This approach thus raises specific issues with respect to the choice of variables to which a common localisation is applied, because mass, wind and humidity fields can have different error characteristics (such as typical scales and possible anisotropy), depending on the choice of corresponding variables ; e.g. either geopotential or temperature ( $T$ ) can be used for the mass field, while for the wind field, either stream function ( $\psi$ ) and velocity potential ( $\chi$ ), either zonal ( $u$ ) and meridional ( $v$ ) wind, or vorticity ( $\zeta$ ) and divergence ( $\eta$ ) are often considered.

## 2) Error characteristics and proposed change of variable for mass and wind

Typical average auto-correlation functions of zonal (respectively meridional) wind components are known to be anisotropic e.g. in the extratropical mid-troposphere (where the flow is predominantly rotational), since they tend to be zonally (respectively meridionally) elongated, in addition to be associated to specific negative lobes on the North and South sides (respectively on the East and West sides) of the considered location at the origin of the auto-correlation function (e.g. Daley 1991). Associated cross-correlation functions between zonal and meridional wind components are also anisotropic for such typical rotational flows, with a zero value at the origin and a quadripole of either positive or negative values at some distance from the origin. Such features indicate that cross-covariances of  $u$  and  $v$  are not well suited for the usual localisation based on separation distance. Different but related characteristics are expected for predominantly divergent flows, and it is only in the case of independent rotational and divergent components with equal amplitudes that zonal and meridional wind components are expected to be isotropic. Typical anisotropic cross-covariances are also classical between e.g. zonal wind and the mass field, due to geostrophic-like effects. These features suggest that zonal and meridional wind components are not much adequate variables for applying the isotropic localisation which is usually employed e.g. in 4DEnVar formulations such as in the Météo-France global model ARPEGE.

For these reasons, either vorticity and divergence, or stream function and velocity potential, are often considered for covariance modelling (e.g. Derber and Bouttier 1999) and for covariance localisation. This is related to the fact that typical average auto-correlation functions of these variables are nearly isotropic for both rotational and divergent flows. However, while typical scales of wind components are relatively similar to those of temperature and specific humidity, stream function and velocity potential are of much larger scale than  $T$ , while vorticity and divergence are of much smaller scale than  $T$ . These scale differences are directly related to the fact that vorticity and divergence (respectively stream function and velocity potential) are spatial derivatives (respectively spatial integrals) of zonal and meridional wind components.

Therefore, it would be desirable to consider wind variables which are nearly isotropic as stream function and velocity potential (and as vorticity and divergence), but which have similar spatial scales as temperature and wind components. Such wind variables can be easily constructed in spectral space for instance, after noticing that e.g. stream function and vorticity are simply related by a Laplacian operator ( $\Delta$ ), whose spectral coefficients  $\Delta_n$  are directly proportional to the square of the total wave number  $n$  (or to  $n(n+1)$  more precisely). This can be expressed as follows in terms of spectral coefficients  $\zeta_{n,m}$  and  $\psi_{n,m}$  (where  $m$  is the zonal wave number) :

$$\zeta_{n,m} = \Delta_n \psi_{n,m}$$

This Laplacian operator implies that the power spectrum of vorticity is related to the power spectrum of stream function roughly multiplied by  $n^4$ , which strongly emphasizes the contribution of large wave numbers to the power spectrum of vorticity. This suggests that isotropic wind variables, with scales intermediate between those of  $(\psi, \chi)$  and  $(\zeta, \eta)$  respectively, may be constructed by applying the square root of the Laplacian operator to stream function and velocity potential. These transformed variables  $\psi'$  and  $\chi'$  may be called “scaled stream function” and “scaled velocity potential” respectively, with their spectral coefficients defined by :

$$(\psi')_{n,m} = (\sqrt{\Delta})_n \psi_{n,m} \quad \text{and} \quad (\chi')_{n,m} = (\sqrt{\Delta})_n \chi_{n,m}$$

This transformation preserves isotropy (because it only depends on  $n$ ), and power spectra of  $\psi'$  and  $\chi'$  are those of  $\psi$  and  $\chi$  roughly multiplied by  $n^2$ . This is thus expected to provide nearly isotropic variables  $\psi'$  and  $\chi'$ , whose scales are similar to those of zonal and meridional wind components.

A similar issue of spatial scale is raised when e.g. the logarithm of surface pressure ( $\ln(P_s)$ ) is considered in

addition to temperature at different vertical levels (e.g. Derber and Bouttier 1999). This logarithm of surface pressure tends to have much larger spatial scales than temperature, so that a transform may also be applied to obtain a variable with similar spatial scales as the other fields. Since surface pressure is strongly related to stream function in nearly geostrophic flows, it can be considered to apply the same square root of the Laplacian operator to  $\ln(P_s)$  as for  $\psi, \chi$  in order to define a similarly scaled variable :  $([\ln(P_s)]')_{n,m} = (\sqrt{\Delta}_n (\ln(P_s)))_{n,m}$ .

### 3) Diagnosis of horizontal localisation scales for scaled variables, and preliminary 4DEnVar experiments

In order to evaluate the adequacy of these scaled variables for applying a common horizontal localisation (at a given vertical level), some localisation length-scales have been diagnosed for a few variables at different vertical levels for the ARPEGE 4DEnVar system (Desroziers et al 2014), using a 200-member ensemble corresponding to random draws from the operational ARPEGE background error covariance matrix. Horizontal localisation length-scales have been here diagnosed using optimality-based localisation diagnostics (Ménétrier et al 2015).

The corresponding vertical profiles of length-scales (Figure 1) indicate that scaled stream function  $\psi'$  and scaled velocity potential  $\chi'$  have similar localisation length-scales as temperature and humidity. A similar result is obtained for the scaled logarithm of surface pressure  $[\ln(P_s)]'$ , whose localisation length-scale is close to those of low-level temperature, whereas the localisation length of  $\ln(P_s)$  is about 5 times larger than for temperature.

Preliminary single-observation assimilation experiments also indicate that e.g. the vertical coupling between low-level temperature and surface pressure is much better preserved when using such scaled variables, due to a more consistent treatment of horizontal localisation scales for surface pressure and temperature. Multivariate relationships such as geostrophy are also expected to be better represented when using these variables, due to underlying nearly isotropic cross-covariances which are more adequately localised. This is supported in the experimental ARPEGE 4DEnVar system, by reduced spinup effects when using scaled variables  $\psi', \chi'$  and  $[\ln(P_s)]'$  instead of  $u, v$  and  $\ln(P_s)$ .

These scaled variables have thus been adopted in current experimentations of the ARPEGE 4DEnVar system which is under development at Météo-France.

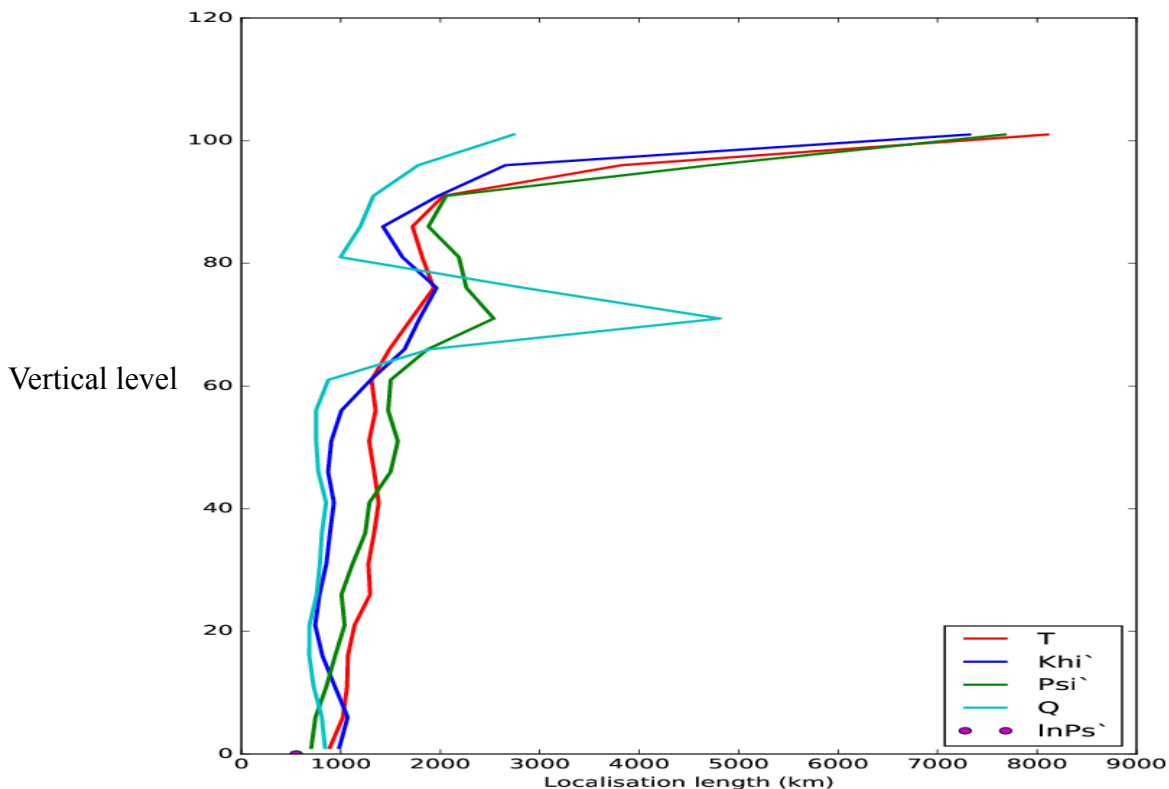


Figure 1: Vertical profile of horizontal localisation length-scales (in m) diagnosed for temperature ( $T$ ), scaled stream function ( $\Psi'$ ), scaled velocity potential ( $Khi'$ ), humidity ( $Q$ ) and scaled logarithm of surface pressure ( $\ln P_s'$ ). An average profile is used in 4DEnVar.

#### References

- Daley, R., 1991 : Atmospheric data analysis. Cambridge University Press, Cambridge, UK, 460 pp.  
 Derber, J. and F. Bouttier 1999 : A reformulation of the background error covariance at ECMWF. *Tellus*, 51A, 195-221.  
 Desroziers, G., Camino, J.-T. and Berre, L. (2014), 4DEnVar: link with 4D state formulation of variational assimilation and different possible implementations. *Q.J.R. Meteorol. Soc.*, 140: 2097–2110.  
 Ménétrier, B., T. Montmerle, Y. Michel, and L. Berre, 2015: Linear Filtering of Sample Covariances for Ensemble-Based Data Assimilation. Part I: Optimality Criteria and Application to Variance Filtering and Covariance Localization. *Mon. Wea. Rev.*, **143**, 1622–1643.

# Use of EFSO for Online Data Assimilation Quality Monitoring and Proactive Quality Control

Tse-Chun Chen <sup>1</sup>, Eugenia Kalnay <sup>1</sup>, and Daisuke Hotta <sup>2</sup>

<sup>1</sup>*University of Maryland, College Park, MD, USA*

<sup>2</sup>*Japan Meteorological Agency, Tokyo, Japan*

*Email: tcchen@umd.edu*

## 1. Introduction

An essential basis of the success of Numerical Weather Prediction (NWP) and Reanalysis is the massive amount of observations, growing in number and quality. Maintaining existing observing systems and developing new ones requires enormous resources, and the usefulness of the observed data should be evaluated. The direct comparison between a control run (with all the observations) and data denial runs known as Observing System Experiments (OSEs) is a straightforward evaluation approach. However, with millions of observation assimilated every 6 hours, this task is very challenging. First, the computationally expensive experiments limit the number of runs needed to separate the impact of observation subsets, so the discernibility is low. Second, the difference between including or not including a subset of observations may be insignificant even for 5-day forecasts, given that there are already a lot of additional observations assimilated. Hence accurate impact estimation of small subsets of observations is virtually impossible. To overcome these difficulties, we propose to use Ensemble Forecast Sensitivity to Observations (EFSO; Kalnay et al., 2012), the ensemble version of the FSO developed by Langland and Baker (2004), that attributes the forecast changes back to each observation using future analysis as verification, and hence provides an efficient estimation of the impact of each observation on the quality of the forecast.

## 2. Efficient Quality Monitoring of Data Assimilation using EFSO

EFSO efficiently quantifies the impact of each observation on any given short period of model forecasts and can be used as an online monitoring tool for the quality of data assimilation. As an example, figure 1 shows the time evolution of total 6-hour impact of each observing systems throughout a 1-month experiment. It is clear that most of the observing systems are beneficial at all times (e.g., the top 3 beneficial systems: commercial aircraft reports, GPSRO, and Radiosondes). However, there are several observing systems with occasional detrimental episodes, namely Profiler winds, PIBAL, Atlas buoy, Dropsondes, NEXRAD winds, and especially MODIS winds. It should be noted that these systems are all beneficial on a monthly average but there are some flow dependent conditions that lead to detrimental impact in certain times and locations. Making use of EFSO, it is possible to quickly identify data assimilation quality dropouts that depend on flow condition and have detrimental impact on the resulting forecasts.

## 3. Proactive Quality Control (PQC) based on EFSO

PQC, the fully flow dependent quality control scheme, was pioneered in Ota (2013) and Hotta (2017), in which EFSO was performed with respect to pre-identified forecast bust region and the regional EFSO-detected detrimental observations were rejected if belonging to net detrimental observing systems. The method (Hotta hereafter) was successful in the original motivation: to avoid occasional forecast busts associated with detrimental observations. We further devised two other data denial strategies, namely THReshold (THR) and Beneficial Growing Mode (BGM), showing that the forecast skill can be improved even further by PQC. In THR, the detrimental observations are rejected if the Moist Total Energy of the error impact is larger than  $10^{-5}$  J·kg<sup>-1</sup>. On the other hand, BGM, motivated by Trevisan (2010), only keeps observations that are beneficial to 6-hr forecasts and continue to be beneficial in 24 hours. We compare

the three methods on 18 cases from Hotta (2017) in figure 2. The global-and-case averaged relative 5-day forecast error reduction, which is verified by its own analysis, by PQC-Hotta, -THR, -BGM methods are ~0.5%, 3%, and 5% respectively. These promising results demonstrate great potential in real applications. In operation, PQC-THR is unable to keep up with the latest forecast release, but it can improve the final analysis instead and thus improve future forecasts. Furthermore, PQC-BGM, which requires analysis 24 hours later and is not feasible in operations, can improve the quality of retrospective analysis products since future observations are available.

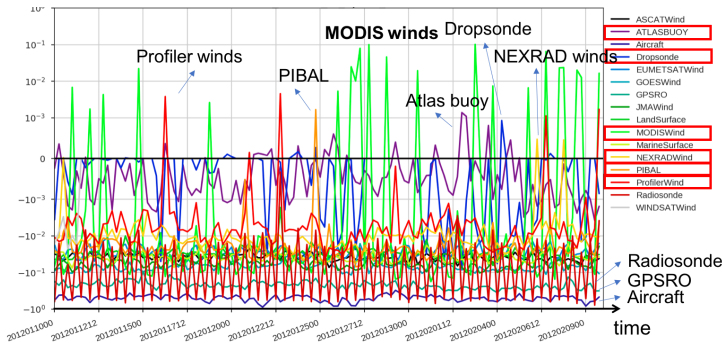


Figure 1. Time evolution of total impact (EFSO) for every non-radiance observation on 6-hour forecasts. Positive values mean the impact of the system is detrimental (marked in red boxes) and negative EFSO means beneficial impact.

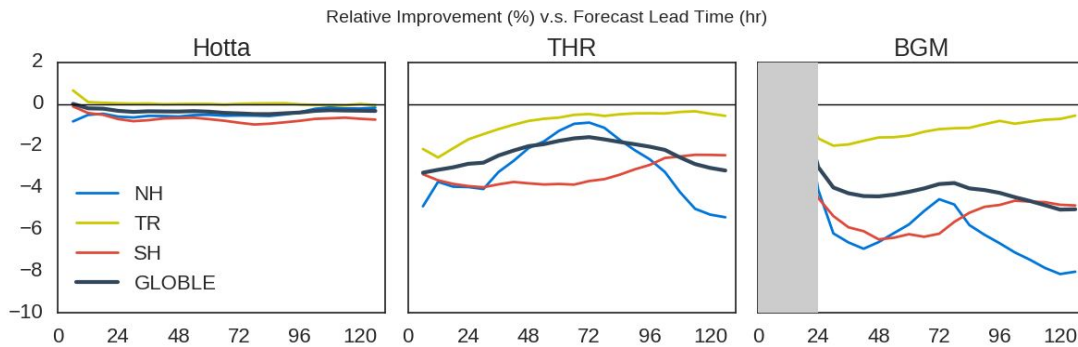


Figure 2. The relative reduction of 5-day forecast errors in %, measured by the Moist Total Energy (MTE) of the forecast error. Left: MTE obtained with the original PQC approach of Ota et al. (2013) and Hotta (2014), which is successful and gives a reduction of O(0.5%). The PQC-THR approach deletes all observations with a detrimental impact of  $10^{-5}$  in MTE units. The PQC-BGM deletes all detrimental observations whose negative impact increases from 6 to 24h. Since it would require a 24h verifying analysis, BGM can only be carried out in a Reanalysis, when future observations and analyses are available.

## References:

- Hotta, Daisuke, Tse-Chun Chen, Eugenia Kalnay, Yoichiro Ota, and Takemasa Miyoshi. 2017. "Proactive QC: A Fully Flow-Dependent Quality Control Scheme Based on EFSO." *Monthly Weather Review*, May, MWR-D-16-0290.1. doi:10.1175/MWR-D-16-0290.1.
- Kalnay, Eugenia, Yoichiro Ota, Takemasa Miyoshi, and Junjie Liu. 2012. "A Simpler Formulation of Forecast Sensitivity to Observations: Application to Ensemble Kalman Filters." *Tellus A* 64 (October). doi:10.3402/tellusa.v64i0.18462.
- Ota, Yoichiro, John C. Derber, Eugenia Kalnay, and Takemasa Miyoshi. 2013. "Ensemble-Based Observation Impact Estimates Using the NCEP GFS." *Tellus A* 65 (September). doi:10.3402/tellusa.v65i0.20038.
- Trevisan, Anna, Massimo D'Isidoro, and Olivier Talagrand. 2010. "Four-Dimensional Variational Assimilation in the Unstable Subspace and the Optimal Subspace Dimension." *Quarterly Journal of the Royal Meteorological Society* 136 (647): 487–96.

# Diagnosis of some error contributions in global and regional data assimilation cycling

Rachida EL OUARAINI<sup>1</sup>, Loïk BERRE<sup>2</sup> and Claude FISCHER<sup>2</sup>

<sup>1</sup>Maroc-Météo, CNRMSI, Casablanca, Morocco ([elouaraini@gmail.com](mailto:elouaraini@gmail.com))

<sup>2</sup>Météo-France, CNRM/GMAP, Toulouse, France

Ensemble data assimilation experiments are often run by perturbing observations and the model in a cycled way. The links between associated ensemble sensitivity experiments and a possible diagnosis of the amplitude of different error contributions are here made explicit and discussed, in the context of both global and regional systems.

## 1. Formal evolution of ensemble perturbations and of errors in data assimilation (DA)

As discussed in El Ouaraini and Berre (2011) and El Ouaraini et al (2015), during a given analysis/forecast step (whose index is denoted by  $l$ , associated to time  $t_l$ ), while the full model state of each ensemble member evolves in a non linear way (due to non linearities of the forecast model in particular), ensemble forecast perturbations  $\tilde{\epsilon}_l^f$  can be formally conceived as resulting from linearized accumulation and propagation of three different contributions (equation (1)) :

$$\tilde{\epsilon}_l^f = \mathbf{T}_{l+1} \tilde{\epsilon}_0^b + \sum_{i=0}^l \mathbf{T}_{l-i} \mathbf{M}_i \mathbf{K}_i \tilde{\epsilon}_i^o + \sum_{i=0}^l \mathbf{T}_{l-i} \tilde{\epsilon}_i^m \quad (1)$$

where  $\tilde{\epsilon}_0^b$ ,  $\tilde{\epsilon}_i^o$  and  $\tilde{\epsilon}_i^m$  correspond respectively to initial background perturbations (introduced at a given initial time  $t_0$ ) and to recent observation perturbations and model perturbations, both introduced at recent successive steps  $t_i$  between  $t_0$  and  $t_l$ . The  $\mathbf{T}$  matrices represent the following cycling operators over several past successive analysis/forecast steps  $j$  :

$$\mathbf{T}_{l+1} = \prod_{j=0}^l \mathbf{M}_j (\mathbf{I} - \mathbf{K}_j \mathbf{H}_j)$$

$$\mathbf{T}_{l-i} = \prod_{j=i}^{l-1} \mathbf{M}_j (\mathbf{I} - \mathbf{K}_j \mathbf{H}_j)$$

where  $\mathbf{M}_j$  is a linearized version of the model operator (around the non linear (unperturbed) deterministic state),  $\mathbf{K}_j$  is the specified gain matrix, and  $\mathbf{H}_j$  is the linearized version of the observation operator.

While this formalism is valid for the evolution of ensemble perturbations, it can also be considered to be representative of the actual error evolution. This means not only that this formalism can be used for investigating some sensitivity of ensemble spread to different perturbation sources (e.g. in order to show that ensemble spread is not much sensitive to old background perturbations, after some spinup period), but it also implies that this formal framework can also be applied to derive estimates of different contributions to the forecast error amplitude. This is illustrated and discussed in the next two sections, using some Figures from El Ouaraini and Berre (2011) in section 2, and from El Ouaraini et al (2015) in section 3. Note that these Figures were discussed in terms of sensitivity experiments in these two papers, while we discuss here their implications with respect to estimation of error contributions.

## 2. Contribution of initial background errors in a global data assimilation system

Figure 1 illustrates the temporal evolution of global spread of vorticity near 500 hPa for a cold-start configuration (solid line, associated to zero values for the initial background perturbations :  $\tilde{\epsilon}_0^b = 0$ ) and for a warm-start configuration (dashed line, corresponding to non-zero values for the initial background perturbations  $\tilde{\epsilon}_0^b$ , thanks to ensemble DA cycling over 6 preceding days) of the ARPEGE global ensemble, in a perfect model framework (i.e.  $\tilde{\epsilon}_i^m = 0$  at every step  $l$ ).

According to equation (1), the difference between the squared values of the two curves in Figure 1 can be interpreted as an estimate of the initial background error contribution (namely  $\mathbf{T}_{l+1} \tilde{\epsilon}_0^b$ ) to the forecast error variance  $V(\tilde{\epsilon}_l^f)$  at different steps  $l$  of the cycling. The results indicate that the initial background error contribution has an amplitude which represents nearly half of the forecast error magnitude at initial time  $t_0$  (while the other half corresponds to the contribution of observation errors introduced at time  $t_0$ ). It also appears that this initial contribution tends to vanish after 3 days of data

assimilation cycling, due to successive analysis damping effects during the cycling. This comparative analysis is thus also a way to study and show to which extent background errors (depending on their “age” with respect to the current cycling step  $l$ ) contribute to uncertainties in the data assimilation cycling.

### 3. Contribution of Lateral Boundary Condition (LBC) errors in a regional data assimilation system

Figure 2 shows the temporal evolution of horizontally averaged analysis spread at 00 UTC for temperature near 850 hPa for the ALADIN-France regional ensemble, using either unperturbed Lateral Boundary Conditions (solid line) or perturbed Lateral Boundary Conditions (dashed line), in a perfect model framework (i.e. model perturbations are equal to zero at every step  $l$ , except for Lateral Boundary Condition perturbations obtained through the coupling to a global ARPEGE ensemble).

According to equation (1), the difference between the squared values of the two curves can be interpreted as the contribution of LBC errors (which are one part of the model errors  $\tilde{\epsilon}_l^m$ ) to forecast error variance (on average over the considered ALADIN-France domain). The results indicate that LBC errors explain about one third of forecast error variance on average over the considered area. As illustrated in Figure 3, this contribution varies much over the domain, with values that tend to be largest near the boundaries and in associated downstream regions. Such sensitivity experiments can thus be explicitly used to investigate the influence of LBC errors on regional forecast error amplitudes.

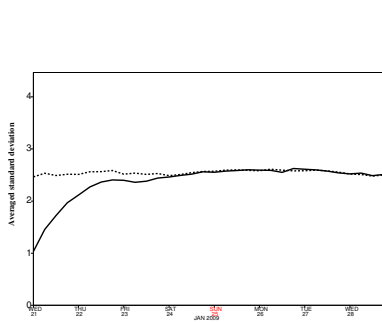


Figure 1: Temporal evolution of global spread of vorticity near 500 hPa for cold-start (solid line) and warm-start (dashed line) configurations of the ARPEGE global ensemble.

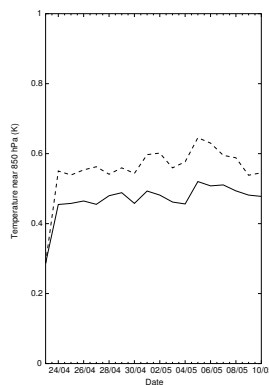


Figure 2: Temporal evolution of horizontally averaged analysis spread at 00 UTC for temperature near 850 hPa for the ALADIN-France regional ensemble, using either unperturbed LBCs (solid line) or perturbed LBCs (dashed line).

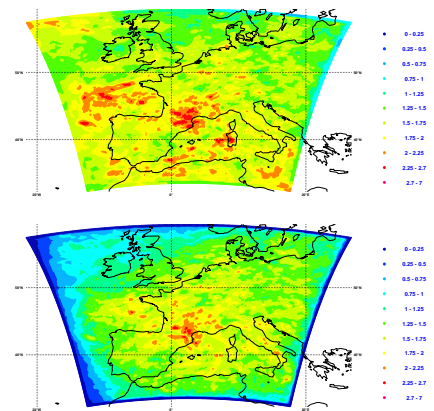


Figure 3: Horizontal maps of time-averaged spread of 6h zonal wind forecasts at 06 UTC, using either unperturbed LBCs (bottom panel) or perturbed LBCs (top panel).

### 4. Conclusions and future work

While sensitivity experiments can be relevant as such in ensemble data assimilation, we advocate their use for additionally deriving explicit estimations of error contributions, in both global and regional data assimilation systems. Such experiments and diagnostics may also be compared with innovation-based estimates in the future, in order to compare and derive estimates of model error contributions for instance.

### References

- [1] El Ouaraini, R. and Berre, L. 2011. Sensitivity of ensemble-based variances to initial background perturbations. *J. Geophys. Res.* 116, D15106. DOI: <http://dx.doi.org/10.1029/2010JD015075>.
- [2] El Ouaraini, R., C. Fischer, L. Berre and EH. Sayouty, 2015. Sensitivity of regional ensemble data assimilation spread to perturbations of lateral boundary conditions. *Tellus A*, 67. DOI: <http://dx.doi.org/10.3402/tellusa.v67.28502>.

# Operational use of Suomi NPP ATMS radiance data in JMA's global NWP system

Yoichi Hirahara, Takumu Egawa and Masahiro Kazumori  
Numerical Prediction Division, Japan Meteorological Agency  
E-mail: hiraharayo@met.kishou.go.jp

## 1. Introduction

Since March 2017, microwave radiance data from the Advanced Technology Microwave Sounder (ATMS) of the Suomi National Polar-orbiting Partnership (NPP) spacecraft have been assimilated operationally into the global Numerical Weather Prediction (NWP) system run by the Japan Meteorological Agency (JMA). This report briefly describes related data quality control and the impacts of the assimilation.

## 2. Methods

The 22-channel ATMS is the successor to the Advanced Microwave Sounding Unit-A (AMSU-A) and Microwave Humidity Sounder (MHS) instruments. For the temperature-sounding channels (6 – 15) of this sounder, an ATOVS and AVHRR Pre-processing Package (AAPP) FFT-based filter is applied to achieve noise performance similar to that of AMSU-A. For ATMS data assimilation into the global NWP system, the approaches used for AMSU-A/MHS quality control (Okamoto et al. 2005) and variational bias correction (Sato 2007, Ishibashi 2009) in the system are applied. The thinning distance is set to 250 km for all ATMS channels. Edge data on field-of-view (FOV) numbers at 1, 2 and 95, 96 are not assimilated due to their anomalous biases. The RTTOV-10 fast radiative transfer model (Saunders et al. 2012) is used for assimilation.

Preliminary experiments involving the assimilation of ATMS tropospheric channels (6 – 9, 18 –

22) and stratospheric channels (10 – 15) were performed, with results showing a negative impact from the ATMS stratospheric channels that increased normalized standard deviations (STDV) of the first-guess (FG) departure from AMSU-A stratospheric channels (9 – 14) (Figure 1 (a), green line). As the cause of this impact remains unclear, ATMS tropospheric channels were selected for assimilation into the global NWP system.

## 3. Impacts on the NWP system

Observing system experiments covering periods of a month in each of boreal summer 2015 and winter 2015 – 2016 were performed to evaluate the impact of ATMS data assimilation into the global NWP system. The control experiment (CNTL) had the same configuration as the operational system as of December 2016. Data from ATMS tropospheric channels (6 – 9, 18 – 22) were added to the operational observation data set in the TEST experiment. Figure 1 shows changes in the normalized standard deviations of the FG departure. Although increased STDV was observed for AMSU-A tropospheric channels 6 and 7, results from the MHS, Advanced Microwave Scanning Radiometer 2 (AMSR2), Global Precipitation Measurement (GPM) Microwave Imager (GMI), Global Navigation Satellite System Radio Occultation (GNSS-RO) and radiosonde temperature observation indicated improved water vapor and temperature data in FG fields. Figure 2 shows the zonal means of root mean square error (RMSE)

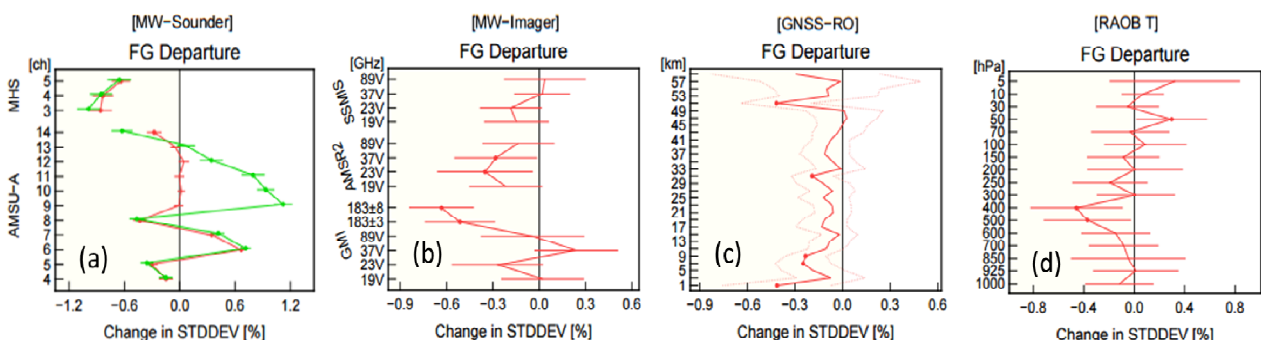


Figure 1: Normalized changes in the STDV of FG departures from (a) AMSU-A and MHS, (b) SSMIS, AMSR2 and GMI, (c) GNSS-RO bending angle and (d) radiosonde temperature observation in the boreal summer experiment. Negative values represent improvement. The horizontal axis indicates differences in normalized standard deviation. Error bars represent a 95% confidence interval, and dots represent statistically significant changes. In panel (a), the green line represents the results of a preliminary test in which stratospheric channels 10 – 15 were included in the assimilation.

differences for geopotential height on day 1 to day 3 forecasts in the boreal summer experiment. Clear positive impacts in the mid- and upper troposphere were observed, especially in the Southern Hemisphere. The assimilation of ATMS radiance data also brought improved tropical cyclone track predictions for the experiment periods (Figure 3).

Based on these findings, ATMS radiance data have been assimilated into JMA's global NWP system since 29 March 2017.

**References**

Ishibashi, T., 2009: Implementation of a new background error covariance matrix in the variational bias

correction scheme for the JMA Global 4D-Var System. *CAS/JSC WGNE Research Activities in Atmospheric and Oceanic Modeling, Rep.*, **39**, 1 – 15.

Okamoto, K., M. Kazumori, and H. Owada, 2005: The Assimilation of ATOVS Radiances in the JMA Global Analysis System. *J. Meteor. Soc.*, **83**, 201 – 217.

Sato, Y., 2007: Introduction of variational bias correction technique into the JMA global data assimilation system. *CAS/JSC WGNE Research Activities in Atmospheric and Oceanic Modeling, Rep.*, **37**, 1 – 19.

Saunders R., J. Hocking, P. Rayer, M. Matricardi, A. Geer, N. Bormann, P. Brunel, F. Karbou and F. Aires, 2012: RTTOV-10 science and validation report. *NWP-SAF Report, Met. Office, UK*, pp. 31.

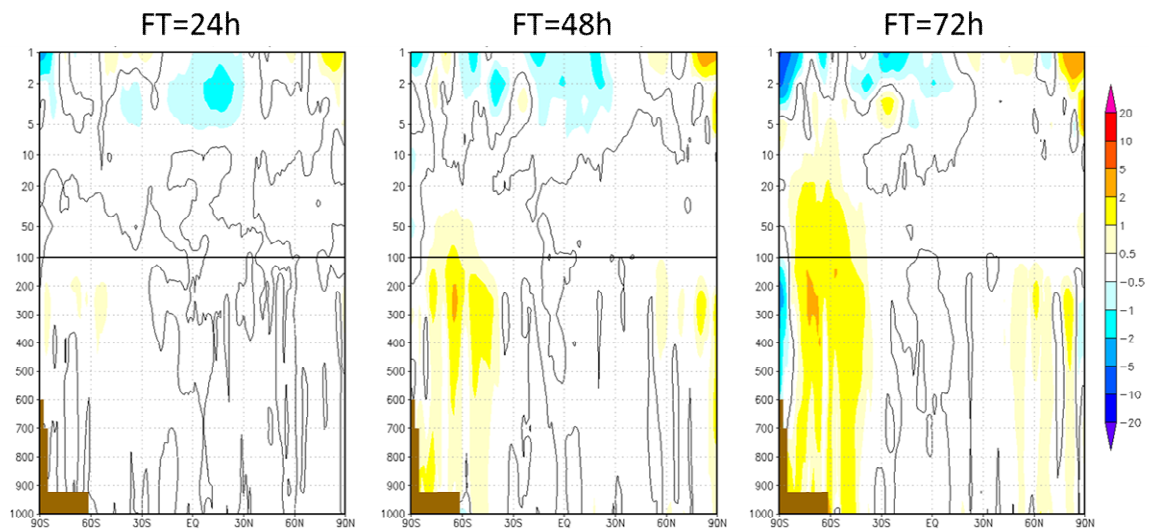


Figure 2: Zonal mean of RMSE differences between CNTL (without ATMS) and TEST (with ATMS) for forecasting of geopotential height in August 2015. Positive values indicate forecast error reductions. Verification is against the experiment's own analysis.

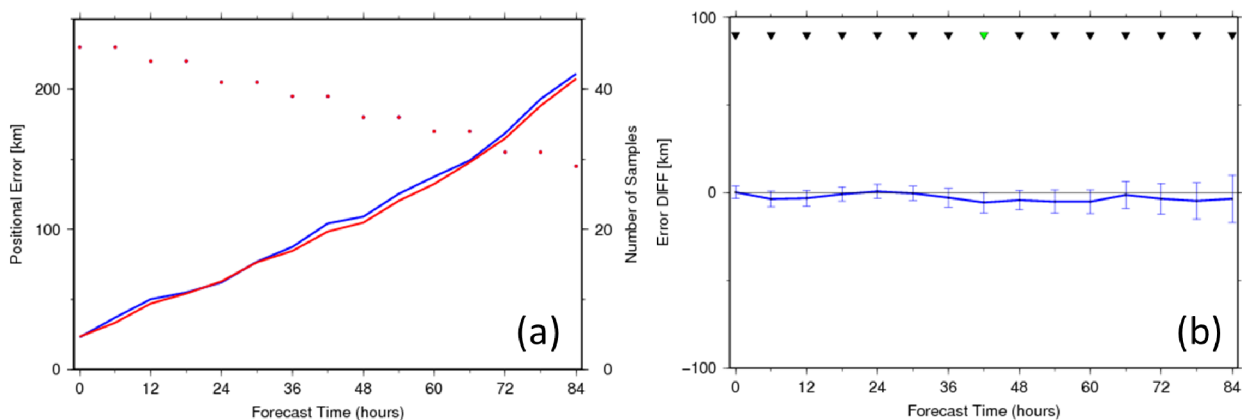


Figure 3: (a) Average of typhoon track forecast errors for August 2015. The red and blue lines represent positional errors of TEST (with ATMS) and CNTL (without ATMS), respectively. Red dots indicate the number of cases included in the statistics. Forecasts were verified against best-track data from Regional Specialized Meteorological Centre (RSMC) Tokyo – Typhoon Center analysis. The horizontal axis indicates forecast time. (b) Difference in typhoon position errors between TEST and CNTL. Negative values indicate error reductions, and error bars represent a 95% confidence interval. The triangles at the top indicate the statistical significance differences, with green indicating significance.

# **Assimilation of GNSS RO data into JMA's mesoscale NWP System**

Yoichi Hirahara, Hiromi Owada, and Masami Moriya

Numerical Prediction Division, Japan Meteorological Agency

E-mail: hiraharayo@met.kishou.go.jp

## **1. Introduction**

The Global Navigation Satellite System (GNSS) forms a very important part of today's meteorological observation network. GNSS Radio Occultation (RO) data exhibit fairly uniform distribution worldwide, in contrast to data from radiosondes and aircraft, producing vertical profiles of atmospheric parameters that can be assimilated into numerical weather prediction (NWP) systems without bias correction. The Japan Meteorological Agency (JMA) has been assimilating RO data into its global NWP system since March 2007, and began using GNSS RO refractivity data in its operational mesoscale NWP system in March 2016. This report outlines the impact of GNSS RO data on JMA's mesoscale NWP system.

## **2. Methods**

In JMA's mesoscale NWP system, RO data from GRACE-A, GRACE-B, Metop-A, Metop-B, COSMIC, TerraSAR-X and TanDEM-X are assimilated after application of gross-error quality checking. The one-dimensional observation operator in the Radio Occultation Processing Package (ROPP) is used for data assimilation.

Assimilation in consideration of bending angles often produces better performance than that based on refractivity data, as the latter is derived from bending angle observation. However, a greater wealth of upper-layer NWP model information is necessary for bending angle assimilation. If the NWP model top is under 10 hPa, the use of refractivity profiles is reasonable (Healy 2008). The model top in the mesoscale NWP system is about 40 hPa. Comparison of experiment results regarding assimilation of RO refractivity and RO bending angle data showed slightly better improvement with the former, while improved first-guess temperature profiles were seen with both, especially in the upper troposphere. These results suggest that the upper-layer information of the current mesoscale model may be insufficient for bending-angle assimilation due to the limited model-top height. Accordingly, RO refractivity data are assimilated into the mesoscale NWP system.

## **3. Impacts on the mesoscale NWP system**

Observing system experiments were performed over periods of a month in each of summer 2015 and winter 2014 – 2015 to evaluate the impacts of RO refractivity data in the mesoscale NWP system. The configuration of the control experiment (CNTL) was the same as that of the operational system, and additional use of RO refractivity data was implemented in the test experiment (TEST). As shown in Figure 1, changes in the normalized standard deviation of the first-guess departure indicate consistent improvement in the temperature field. Figure 2 shows profiles of mean errors (ME) and root mean square errors (RMSE) against the radiosonde observation of geopotential height. The ME and RMSE reductions are particularly remarkable around the upper troposphere. This improvement covered a lead time of around 21 hours.

Based on these findings, RO refractivity data were assimilated into JMA's operational mesoscale NWP systems as of 24 March 2016.

## References

Healy, S., 2008: Assimilation of GPS radio occultation measurements at ECMWF. *Proceedings of the GRAS SAF Workshop on Applications of GPS Radio Occultation Measurements, ECMWF, June 16 – 18.*

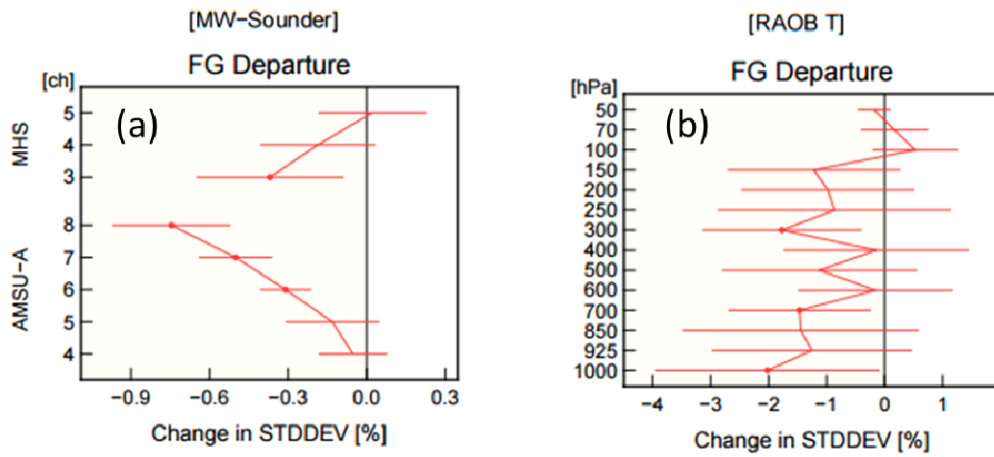


Figure 1: Normalized changes in the standard deviation of first-guess departures from (a) AMSU-A and MHS and (b) radiosonde temperature observation in the summer 2015 experiment. Negative values represent improvement. The horizontal axis indicates normalized STDV differences, error bars represent a 95% confidence interval, and red dots represent statistical significance.

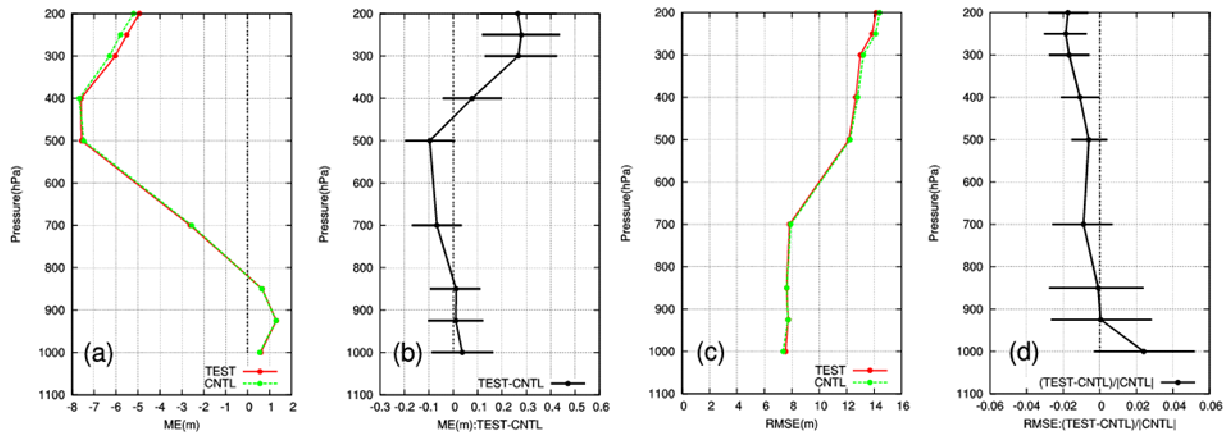


Figure 2: Fits to RAOB for 21-hour forecasting of geopotential height from the summer 2015 experiment. (a) Vertical profile of ME, (b) TEST-CNTL of ME, (c) vertical profile of RMSE, (d) rate of RMSE change  $((\text{TEST}-\text{CNTL})/|\text{CNTL}|)$ . The red and green lines represent TEST and CNTL, respectively, and error bars represent a 95% confidence interval.

# Assimilation of Suomi NPP/CrIS radiance data into JMA's global NWP system

Norio Kamekawa, Masahiro Kazumori

Numerical Prediction Division, Forecast Department, Japan Meteorological Agency  
1-3-4 Otemachi, Chiyoda-ku, Tokyo, 100-8122, Japan

E-mail: orion-kamekawa@met.kishou.go.jp, kazumori@met.kishou.go.jp

## 1. Introduction

Hyper Spectral Infrared Sounder (HSS) radiance data from the Cross-track Infrared Sounder (CrIS) on the Suomi National Polar-orbiting Partnership (NPP) spacecraft have been operationally assimilated into the global Numerical Weather Prediction (NWP) system run by the Japan Meteorological Agency (JMA) since March 2017. This report briefly describes related data quality control and the impacts of assimilation.

## 2. Quality control

The CrIS instrument is a Fourier transform spectrometer with a total of 1,305 infrared sounding channels covering three bands (i.e., the long-wave ( $655 - 1,095 \text{ cm}^{-1}$ ), mid-wave ( $1,210 - 1,750 \text{ cm}^{-1}$ ) and short-wave ( $2,155 - 2,550 \text{ cm}^{-1}$ ) spectral ranges). JMA obtains the CrIS 399-channel data set from NESDIS (the National Environmental Satellite, Data, and Information Service). 27 long-wave temperature sounding channels were selected for use in assimilation. As Aqua/AIRS and Suomi NPP/CrIS are in the same 13:30 afternoon satellite orbit, data thinning is necessary for the overlap region to reduce overfitting in analysis. Normally, higher priority in data thinning is assigned to CrIS due to its wider swath coverage (CrIS: 2,230 km; AIRS: 1,650 km). Priority in such thinning depends on available channel numbers (i.e., clear-sky conditions) and the distance between the observation and the center of the thinning grid box. CrIS data for particular FOV (field of view) numbers (1, 3, 5, 7 and 9) are rejected for assimilation due to their anomalous biases. The method of cloud top estimation and cloud screening proposed by Eyre and Menzel (1989), which is already implemented in the operational system for AIRS and IASI data processing, is applied to CrIS data.

## 3. Assimilation experiments

Observing system experiments covering periods of a month in each of boreal summer 2015 and winter 2015 – 2016 were performed to evaluate the impacts of CrIS data assimilation into the global NWP system. The control experiment (CNTL) had the same configuration as the operational system. In the test experiment (TEST), CrIS data were added on top of the operational observation dataset.

As shown in Figure 1, changes in the normalized standard deviation of the first-guess departure (FG) in the Southern Hemisphere indicate improvement of temperature fields in the stratosphere and the upper troposphere for the combined experiment period of summer and winter. Figure 2 shows improvement of geopotential height forecasts for the stratosphere and the upper troposphere, especially in summer over the Southern Hemisphere.

#### 4. Summary

Results from assimilation experiments conducted to evaluate CrIS radiance data assimilation into JMA's global system showed that the addition of CrIS long-wave temperature sounding channels produced clear improvement of temperature analysis for the upper troposphere and stratosphere. Significant improvement of geopotential height forecasting for the Southern Hemisphere was also confirmed. Based on these findings, CrIS radiance data have been assimilated into JMA's global NWP system since 29 March 2017.

#### References

Eyre, J. R. and W. P. Menzel, 1989: Retrieval of Cloud Parameters from Satellite Sounder Data: A Simulation Study. *J. Appl. Meteor. Climat.*, 267 – 275.

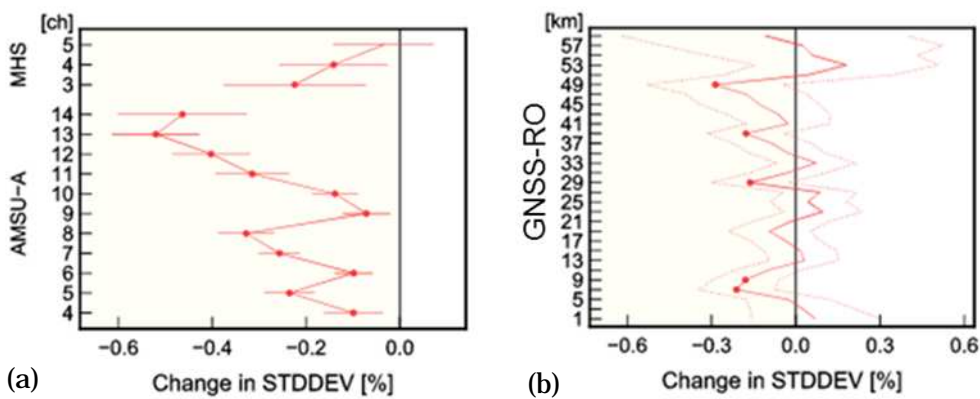


Figure 1. Normalized changes in the standard deviation of FG departures for (a) AMSU-A and MHS and (b) GNSS-RO bending angle for the combined experiment period of summer and winter. Negative values represent improvement. The horizontal axis indicates differences in normalized standard deviation. Error bars represent a 95% confidence interval, and red dots represent statistically significant changes.

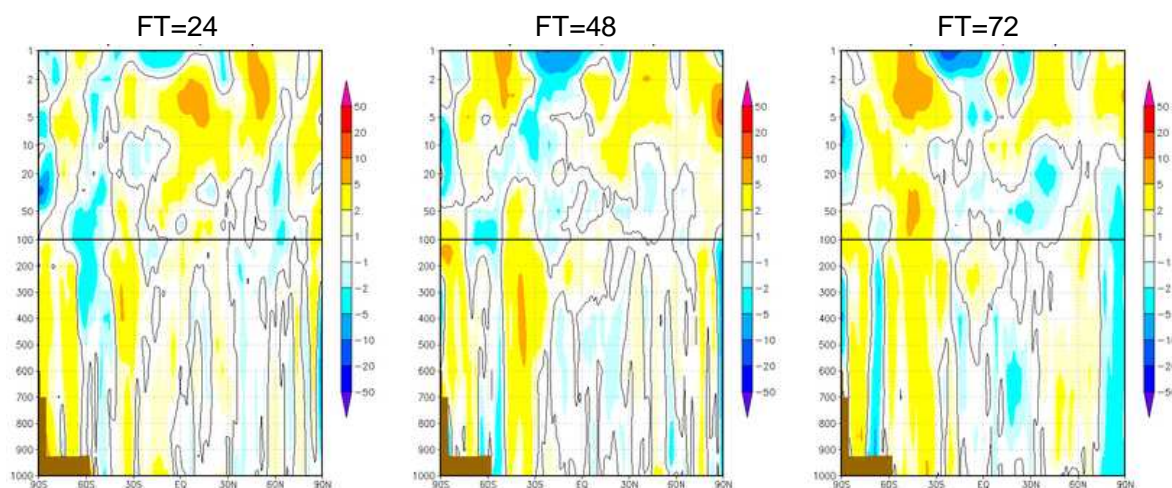


Figure 2. Improvement ratio  $((\text{CNTL} - \text{TEST}) / \text{CNTL})$  for zonal mean of differences in RMS error for geopotential height forecasting in August 2015. Positive values indicate forecast error reductions. Verification is against the experiment's own analysis.

# Assimilation of SSMIS humidity sounding channels into JMA's global NWP system

Yasutaka Murakami and Masahiro Kazumori

Numerical Prediction Division, Forecast Department, Japan Meteorological Agency

Corresponding author: Y. Murakami, JMA, 1-3-4 Otemachi, Chiyoda-ku, Tokyo, 100-8122, Japan

E-mail: y\_murakami@met.kishou.go.jp

## 1. Introduction

Satellite microwave radiance observation provides information on atmospheric temperature and moisture for numerical weather prediction (NWP) models. In this context, the Japan Meteorological Agency (JMA) utilizes clear-sky radiance data from the MHS<sup>1</sup> onboard NOAA<sup>2</sup>-18, NOAA-19, MetOp<sup>3</sup>-A and MetOp-B satellite, SAPHIR<sup>4</sup> onboard Megha-Tropiques satellite, and GMI<sup>5</sup> onboard GPM<sup>6</sup>-core satellite in its global data assimilation system. In addition, JMA began utilizing humidity sounding channels from Special Sensor Microwave Imager/Sounder (SSMIS) onboard DMSP<sup>7</sup> F-17 and F-18 satellite in March 2017. Assimilated SSMIS humidity sounding channels (i.e., those located around the 183-GHz water vapor absorption line) are calibrated with the Unified Preprocessor Package (UPP) (Bell et al. 2008). Assimilating SSMIS UPP humidity sounding channels into the system helps to fill gaps among other humidity sounding data coverage areas. This report describes the SSMIS humidity sounding channel assimilation procedure and the resulting impacts on analysis and forecasts.

## 2. Methodology

It is crucial to detect and discriminate data affected by cloud and precipitation in clear-sky assimilation because the effects of cloud liquid water emission and freezing-particle scattering are not considered in radiative transfer calculation for data assimilation. Oceanic SSMIS UPP data are used because ocean surface emissivity estimation is relatively accurate, whereas estimation of land and sea ice surface emissivity is challenging due to inhomogeneity and seasonal dependence. The use of oceanic data allows analysis to determine the effects of liquid and frozen hydrometeor particles without consideration of complex surface contributions. Expertise gained from research and development on a cloud screening method for assimilation with 24 SSMIS observation channels is expected to support the future development of all-sky microwave radiance assimilation.

A new algorithm detects cloud-affected SSMIS data by classifying such information into three categories based on hydrometeor types (i.e., cloud liquid particles, snow crystals and ice crystals). The determination of each cloud type is based on retrieved cloud liquid water (CLW), the polarization-corrected brightness temperature (Spencer et al., 1986), which involves the use of low-frequency channels, and the scattering index (Ferraro et al., 2000), which involves the use of high-frequency channels. The approach of Weng et al. (1997) is applied for CLW retrieval.

In JMA's global data assimilation system, the variational bias correction (VarBC) scheme (Sato 2007, Ishibshi 2009) is applied for radiance bias correction. Microwave humidity sounding data are also thinned with a distance value of 180 km.

## 3. Impacts on the NWP system

The impacts of SSMIS UPP data assimilation in JMA's global NWP system were assessed in two observing system experiments (OSEs) covering the one-month periods of August 2015 and January 2016. The results showed improved model first-guess (FG) fits to existing MHS and SAPHIR observations, which are sensitive to atmospheric moisture, indicating consistent improvement in the quality of the model FG water vapor field (Figure 1). The impact of SSMIS UPP data on forecast skill was neutral in the January 2016 experiment (figure not shown). In the August 2015 experiment, positive impact on skill in forecasting the geopotential height field over the Southern Hemisphere was observed (Figure 2).

## 4. Summary

A cloud detection algorithm for the clear-sky assimilation of SSMIS humidity sounding channels was developed and implemented in JMA's global NWP system. The algorithm was effective for the screening of cloud-affected data. OSE results showed that the use of SSMIS UPP data improved the FG water vapor field and geopotential height forecast skill for the Southern Hemisphere in the January 2016 experiment. Based on these findings, assimilation of SSMIS humidity sounding data into JMA's global NWP system was begun in March 2017.

## References

- Bell, W., and Coauthors, 2008: The assimilation of SSMIS radiances in numerical weather prediction models. *IEEE Trans. Geosci. Remote Sens.*, **4**, 884–900.
- Ferraro, R. R., F. Weng, N. C. Grody, and L. Zhao, 2000: Precipitation characteristics over land from NOAA-15 AMSU Sensor, *Geophys. Res. Lett.*, **27** (17), 2669–2672.
- Ishibashi, T., 2009: Implementation of a new back-ground error covariance matrix in the variational bias correction scheme for the JMA Global 4D-Var System. *CAS/JSC WGNE Research Activities in Atmospheric and Oceanic Modeling, Rep.*, **39**, 1-15.
- Sato, Y., 2007: Introduction of variational bias correction technique into JMA global data assimilation system. *CAS/JSC WGNE Research Activities in Atmospheric and Oceanic Modeling, Rep.*, **37**, 1-19.
- Spencer, R. W., M. R. Howland, and D. A. Santek, 1987: Severe storm identification with satellite microwave radiometry: An initial investigation with Nimbus-7 SMMR data. *J. Climate Appl. Meteor.*, **26**, 749–754.
- Weng, F., N. C. Grody, R. Ferraro, A. Basist, and D. Forsyth, 1997: Cloud liquid water climatology from the Special Sensor Microwave/Imager. *J. Climate*, **10**, 1086–1098.

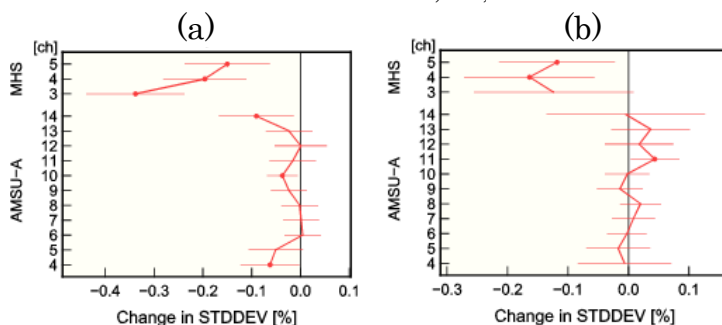


Figure 1. Normalized changes in the standard deviation of FG departures to MHS and AMSU-A for (a) the experiment of August 2015 and (b) that of January 2016. Negative values indicate FG field improvements.

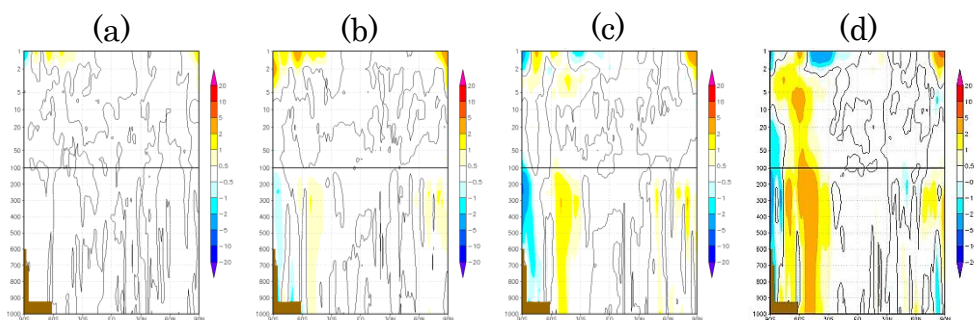


Figure 2. Latitude-Altitude cross section of changes in RMSE of geopotential height fields for (a) 24-hour forecast, (b) 48-hour forecast, (c) 72-hour forecast, (d) 96-hour forecast. Warm colors indicate improvement in the forecast skill.

<sup>1</sup> MHS: Microwave Humidity Sounder  
<sup>2</sup> NOAA: National Oceanic and Atmospheric Administration  
<sup>3</sup> MetOp: Meteorological Operations  
<sup>4</sup> SAPHIR: Sounder for Probing Vertical Profiles of Humidity  
<sup>5</sup> GMI: GPM Microwave Imager  
<sup>6</sup> GPM: Global Precipitation Measurement  
<sup>7</sup> DMSP: Defense Meteorological Satellite Program

## Covariance operators on the equiangular gnomonic cubic grid

R. James Purser, Miodrag Rančić, Manual de Ponca, and David F. Parrish  
NOAA/NCEP/EMC, College Park, MD 20740-3818, U.S.A. (Email: jim.purser@noaa.gov)

### 1. INTRODUCTION

The next operational global forecasting system at NCEP will employ the FV3 dynamical core developed at NASA/GSPC and NOAA/GFDL by Lin and his colleagues (Lin and Rood, 1996; Putman and Lin, 2007) and it will become necessary to adapt NCEP's existing Global Statistical Interpolation (GSI) data assimilation system to the new grid framework employed by the FV3. The most challenging part of this task will be the reformulation of the spatial covariance operators. The grid framework is that of the gnomonic cubed sphere, shown schematically in the figure. The attractive properties of the grid are that, in each of its six tiles, it is free of singularities or significant curvature, and its resolution is almost uniform. But a characteristic feature of that grid that needs to be taken into account in the course of formulating suitable spatial covariance operators is its inherent obliquity, varying with distance from the median lines of each tile and becoming as large as  $120^\circ$  at the grid corners.

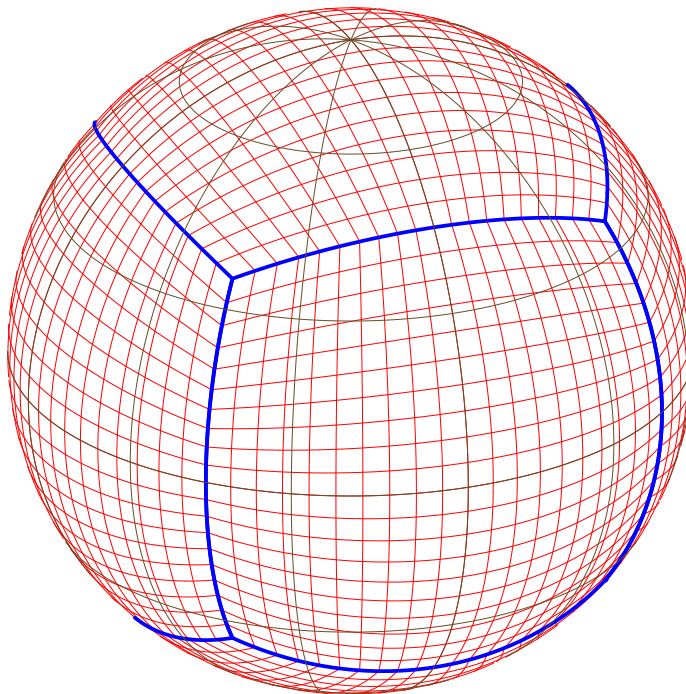


Figure 1. Schematic illustration of the equiangular gnomonic cubed-sphere grid, showing its characteristic weak nonorthogonality.

At present the global GSI covariances are generated on overlapping orthogonal grids (two polar stereographic, sandwiching one nonpolar cylindrical) using the method of sequential spatially-recursive filter as described in, for example, Purser et al. (2003). In the new configuration, a single type of grid suffices, but six copies of it entails some additional interpolation

and blending. The nonorthogonality can be accommodated by augmenting the set of line directions of the one-dimensional smoothers to include the principal grid diagonals as well as just the two main grid directions in the horizontal; essentially this method is already used in NCEP’s operational Real Time Mesoscale Analysis (RTMA, see de Pondeca et al., 2011) to achieve general horizontal anisotropy in an orthogonal grid, whereas we now seek, conversely, to achieve isotropy from a grid that is oblique.

We intend to take the opportunity to investigate whether the recursive filters, with their inconvenient infinite impulse-response, can be replaced with alternative quasi-Gaussian smoothers based on B-splines (de Boor, 1978), whose contrasting finite impulse-response should obviate the need for the massive and non-scalable data motion that the present methods of parallelization involves. Another opportunity suggested by the geometrical simplicity and regularity of the new grid is to adopt an explicitly “multigrid” approach to the additive synthesis of the covariances from many isotropic Gaussian components covering a broad range of scales. By suitably weighting each such component, we gain more flexible control over the covariance profile shape than is feasible in the GSI as presently formulated.

#### REFERENCES

- |   |      |  |
|---|------|--|
| de Boor, C.   | 1978 | <i>A Practical Guide to Splines</i> . Springer, New York. 392 pp.  |
| Lin, S.-J., and R. B. Rood                                      | 1996 | Multidimensional flux-form semi-Lagrangian transport schemes. <i>Mon. Wea. Rev.</i> , <b>124</b> , 2046–2070.  |
| de Pondeca, M. S. F. V., and<br>Coauthors                       | 2011 | The Real-Time Mesoscale Analysis at NOAAs National Centers for Environmental Prediction: Current Status and Development. <i>Wea. Forecasting</i> , <b>26</b> , 593-612.  |
| Purser, R. J., W.-S. Wu, D.<br>F. Parrish, and N. M.<br>Roberts | 2003 | Numerical aspects of the application of recursive filters to variational statistical analysis. Part II: Spatially inhomogeneous and anisotropic general covariances. <i>Mon. Wea. Rev.</i> , <b>131</b> , 1536–1548. |
| Putman, W. M., and S.-J.<br>Lin                                 | 2007 | Finite-volume transport on various cubed-sphere grids. <i>J. Comput. Phys.</i> , <b>227</b> , 55–78.   |

# Developments in Variational Quality Control

R. James Purser, Xiujuan Su, Runhua Yang, and Yanqiu Zhu

NOAA/NCEP/EMC, College Park, MD 20740-3818, U.S.A. (Email: jim.purser@noaa.gov)

## 1. INTRODUCTION

The underlying principle of variational quality control (VQC) is the realistic assumption that actual errors (including those representation errors attributable to the limitations of resolution) of meteorological measurements used to drive a data assimilation deviate from Gaussianity by having distinctly heavier tails (Purser, 1984; Lorenc and Hammon, 1988; Andersson and Järvinen, 1999). The Bayesian implications for a variational assimilation that seeks to minimize the cost function in the form of the negative log-posterior probability density is that the measurements should be adaptively down-weighted when their departures ('O-A') from the analysis to which they are contributing become relatively large.

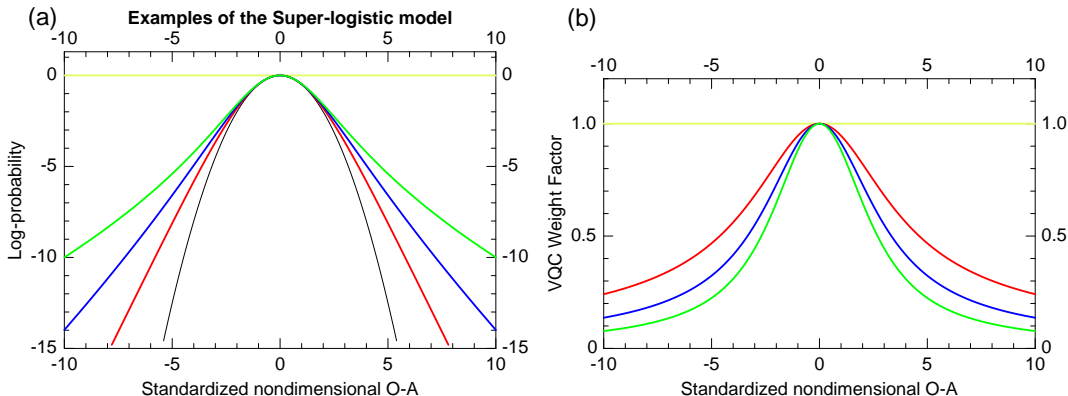


Figure 1. Examples of the standardized forms of the super-logistic model with neutral tail convexity (red), and increasing amounts of negative convexity (blue and green). Panel (a) shows the log-probability densities, with the Gaussian case included for comparison as the black parabolic curve, while panel (b) shows the profile, also as a function of the standardized O-A, of each corresponding weight factor. The effective weight of a measurement used in the assimilation is the product of this factor and its nominal weight.

## 2. NEW DEVELOPMENTS

We have recently explored the use of a probability model for measurement errors based on a generalization, described in Purser (2011), of the logistic distribution. The classical logistic, or ‘sech-squared’, density has a convex log-probability profile which resembles the Huber distributions of Tavolato and Isaksen (2014), so that it is incapable of producing multiple minima in the cost function (unlike the constant-plus-Gaussian model of the earliest VQC schemes), and it also seems to fit the error-distributions of many real data types better. However, for some data, the shapes of the tails of the distributions indicate that at least a small degree of concavity is needed, and this is accommodated by the ‘super-logistic’ generalization of Purser (2011) that we are presently testing within NCEP’s Gridpoint Statistical Interpolation. The figure shows examples of the super-logistic model’s log-probability with varying degrees of the prescribed

convexity (panel a) together with the corresponding effect on the multiplicative factor (panel b) by which the measurements are down-weighted from their standard (Gaussian model) precision weight. The potential risks associated with multiple minima in the cost function will be mitigated in practice by running the first several iterations of the minimization of the cost function using a temporarily neutral convexity parameter, i.e., the ordinary logistic model.

A further development, which the generalization of the logistic model allows us to explore, is the application of these statistical principles to series of coupled measurements. If a set of measurements are assumed to have been made with the same instrument, the detection of a likely gross error in just one of the measurements (an excessively large O-A) can be used to infer a needed down-weighting, not only of itself, but also of its related neighbors even when their own O-A diagnostics alone, are not sufficiently deviant to detect the problem. There are both *in situ* and satellite data types where such an implicit coupling of gross error effects could prove beneficial to the production of more robust and reliable assimilations.

#### REFERENCES

- |                                |      |   |
|--------------------------------|------|---|
| Andersson, E., and H. Järvinen | 1999 | Variational quality control. <i>Quart. J. Roy. Meteor. Soc.</i> , <b>125</b> , 697–722.   |
| Lorenc, A. C., and O. Hammon   | 1988 | Objective quality control of observations using Bayesian methods. Theory and a practical implementation. <i>Quart. J. Roy. Meteor. Soc.</i> , <b>114</b> , 515–543.   |
| Purser, R. J.                  | 1984 | A new approach to the optimal assimilation of meteorological data by iterative Bayesian analysis. <i>Preprint, AMS 10th Conference on Weather Forecasting and Analysis</i> , Clearwater Beach, Florida, pp 102–105.   |
| Purser, R. J.                  | 2011 | Mathematical principles of the construction and characterization of a parameterized family of Gaussian mixture distributions suitable to serve as models for the probability distributions of measurement errors in nonlinear quality control. NOAA/NCEP Office Note 468. |
| Tavolato, C., and L. Isaksen   | 2014 | On the use of a Huber norm for observation quality control in the ECMWF 4D-Var. <i>Quart. J. Roy. Meteor. Soc.</i> , <b>141</b> , 1514–1527.  |

# A Hierarchical Bayes Ensemble Filter

Michael Tsyrlunikov and Alexander Rakitko

*HydroMetCenter of Russia*

Email: michael.tsyrlunikov@gmail.com

## Introduction

In the EnKF, the prior covariances (the  $\mathbf{B}$  matrix) cannot be accurately estimated from a small affordable background ensemble. Errors in the ensemble sample covariances are normally mitigated by a number of ad-hoc devices like covariance localization, variance inflation, and mixing with climatological covariances. In a new Hierarchical Bayes Ensemble (Kalman) Filter, termed HBEF, we propose an objective Bayesian estimation technique for  $\mathbf{B}$ . The HBEF advances the EnKF methodology by introducing a full-fledged secondary filter, which treats the prior covariances like the traditional EnKF treats the state vector.

## Methodology

The HBEF introduces a forecast-analysis update cycle for the prior covariances. At the analysis step, the  $\mathbf{B}$  matrix is estimated using a background for  $\mathbf{B}$  ( $\mathbf{B}^f$ , provided by the forecast step) and the ensemble. To combine the information from  $\mathbf{B}^f$  and from the ensemble members, a hyperprior probability distribution for  $\mathbf{B}$  is introduced. The Inverse Wishart matrix variate probability distribution is used as the hyperprior distribution. The hyperprior distribution is updated in the analysis using the Bayes theorem, with the ensemble members treated as generalized observations on  $\mathbf{B}$ . This leads to an EnVar like analysis algorithm. The posterior mean  $\mathbf{B}$  is computed and propagated at the forecast step to the next analysis time using persistence or regression to climatology.

## Results

The below Figures present results for the one-variable doubly stochastic model of truth. The model is a first-order auto-regression forced by the white noise; the coefficients of the auto-regression are random processes by themselves governed by their own first-order auto-regressions but with constant coefficients. The model is designed to exhibit intermittent instability. The solution of the model equation is a non-stationary random process with the tunable degree of non-stationarity.

Figure 1 shows the analysis RMSEs (w.r.t. the known “truth”, the averaging was over  $2 \cdot 10^5$  assimilation cycles) as functions of the ensemble size  $N$  for several filters (with the analysis RMSE of the unbeatable benchmark Kalman Filter subtracted). One can see that the HBEF was by far better than the (stochastic) EnKF and the variational (Var) filter. For small  $N < 5$ , the Var became more competitive than the EnKF, but still substantially worse than the HBEF.

The HBEF has also been tested with a doubly stochastic advection-diffusion-decay model on the circle, with similar results.

An important advantage of doubly stochastic models is that they allow the estimation of the *true* signal, forecast-error, and analysis-error probability distribution—in particular, signal and error variances—for each time instant separately (signal and error “statistics of the day”). The estimated true error variances can be compared with the respective variances produced by the filter. The estimated systematic errors (biases) in the forecast-ensemble sample variances are presented in Fig.2. One can see that, first, the biases in the ensemble variances were mostly

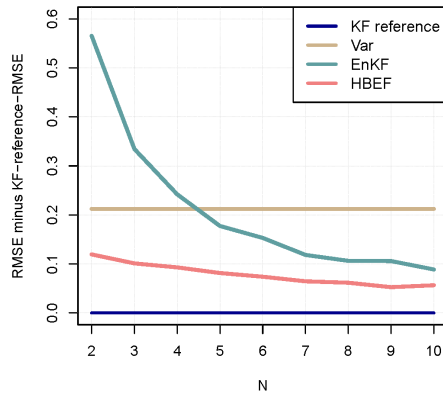


Figure 1: Analysis RMSEs for several filters as functions of the ensemble size  $N$ .

negative for both filters. Second, they were larger when the true variances were larger. Third, the biases for the HBEF were significantly less than those for the EnKF.

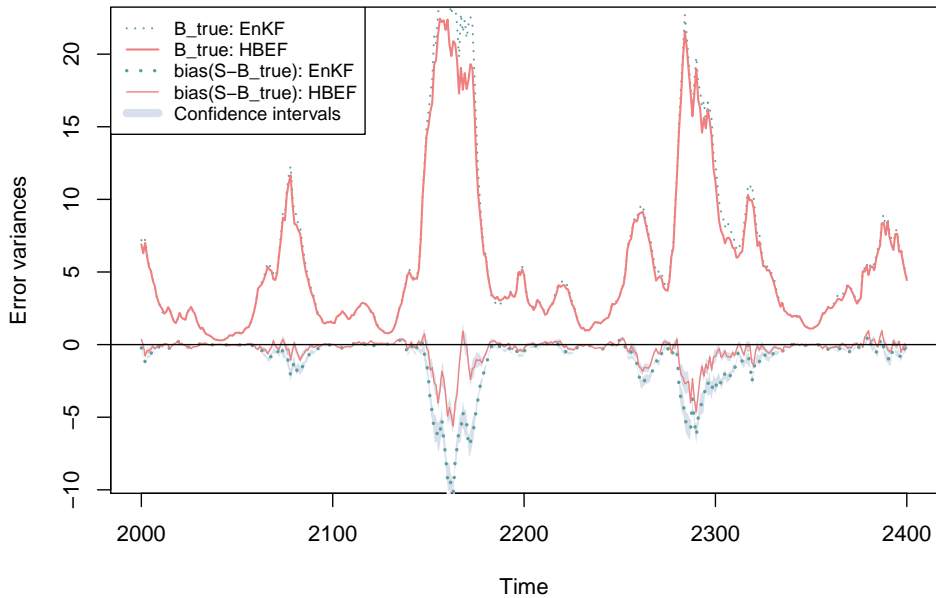


Figure 2: Segments of the time series: the true error variances for EnKF and HBEF (two upper curves) and the *biases* (with the 95% confidence intervals) in the forecast ensemble variances (two lower curves).

For a full exposition, see Tsyrlunikov and Rakitko (2017).

## Bibliography

M. Tsyrlunikov and A. Rakitko. A hierarchical Bayes ensemble Kalman filter. *Physica D (Nonlinear Phenomena)*, 338:1–16, 2017.

# Impacts on local heavy rainfalls of surface winds measurement by seabirds

Akiyoshi Wada<sup>1\*</sup>, Masaru Kunii<sup>1</sup>, Yoshinari Yonehara<sup>2</sup> and Katsufumi Sato<sup>2</sup>

<sup>1</sup>Meteorological Research Institute, Tsukuba, Ibaraki, 305-0052, JAPAN

<sup>2</sup>Atmosphere and Ocean Research Institute, The University of Tokyo, Kashiwa, Chiba 277-8564, JAPAN

\*awada@mri-jma.go.jp

## 1. Introduction

Observations in the surface boundary layer over the ocean are valuable because of rarity. In addition, the vertical profile of winds near the sea surface is not well known so that the Monin-Obukhov similarity theory is used in the atmosphere model. A recent study of Yonehara et al. (2016) reported a new method for the estimation of surface winds by observations of seabirds soaring over the sea. We used a bird-based wind dataset to study the impact of surface winds measurement on the September 2015 Heavy Rainfall Event in Tohoku Regions using the local ensemble transform Kalman filter (LETKF) implemented with the nonhydrostatic model (NHM) developed by the Japan Meteorological Agency (JMA)(Kunii, 2014).

## 2. Data and method

Data assimilation experiments were conducted by using NHM-LETKF. The specification is shown in Table 1. Yonehara et al. (2016) reported a method to estimate wind velocity from Global Positioning System (GPS) track data (one second interval) of soaring seabirds by taking into account the effect of wind drift to the ground velocity of the birds. This method was applied to the track of three streaked shearwaters released in September 2015 to obtain wind's guess data per five minutes when the bird was flying. The period was from 2000UTC 9 to 2100 UTC 10 in September. 10-m wind data was estimated based on the similarity theory and were used for assimilation in the test experiment (TEST), while the control experiment (CTL) was conducted by the NHM-LETKF without wind data by seabirds soaring (Table 2). Mesoscale Analysis (MA) dataset and Comprehensive Database for Assimilation (CDA) archived in JMA were used in both experiments.

Observation data within  $\pm 5$  minutes at the reference time of each cycle were averaged over the model grid spacing because of the horizontal resolution of 15 km and the assimilation interval of 1 hour. The data used in the TEST experiment were regarded as super observations. The observation error was preliminarily set to  $1.0 \text{ ms}^{-1}$ , which is the same as the error of the other typical in situ observations.

Forecast experiments were performed by a 3-km mesh atmosphere-wave-ocean coupled model based on the NHM (Wada et al., 2010). The initial time was 1200 UTC 10 September in 2015 and the integration time was 36 hours. The grid size was  $1141 \times 961 \times 55$ . The time step of the NHM was 4 seconds, that of the ocean model was 24 seconds and that of the ocean wave model was 10 minutes. Atmospheric initial and boundary conditions were created from the analysis in the CTL and TEST experiments, respectively. Oceanic initial conditions were obtained from the objective analysis of JMA with the horizontal resolution of  $0.5^\circ$  in the latitude-longitude coordinate system.

## 3. Results

### 3.1 Impacts for analysis on surface winds

Figure 1a shows the horizontal distribution of the trajectory of three seabirds during the observation period. In situ surface winds were obtained along the east coast of Tohoku Region. Figures 1b-e show the horizontal distributions of the difference in surface winds between CTL and TEST experiments at 0600 UTC (Figures 1b-c) and 1800 UTC (Figures 1d-e) on 10 September. At 0600 UTC, the difference appears east of Tohoku Region with the amplitude less than  $3 \text{ m s}^{-1}$ . The area of the difference with the amplitude higher than  $1 \text{ m s}^{-1}$  shifted eastward where the extratropical

Table1 NHM-LETKF specifications

Ensemble size	50
Grid size	$273 \times 221 \times 50$ ( $\Delta x = 15 \text{ km}$ )
Covariance inflation	relaxation-to-prior spread (Whitaker and Hamill 2012)
Covariance localization	Horizontal 200 km, Vertical $0.2 \ln p$
Analyzed variables	$u, v, w, t, p, q_v, q_c, q_r, q_{ci}, q_s, q_g$
Extended forecast	$817 \times 661 \times 50$ ( $\Delta x = 5 \text{ km}$ ), up to 48 hours

Table 2 Experiments

Experiment	Observations
CTL	MA CDA4
TEST	MA CDA4 + winds by seabirds soaring

cyclone transited from Typhoon Etou existed as if the difference was propagated by environmental flow enhanced by Typhoon Kilo. However, the amplitude of the difference decreased with time. In addition, the seabird winds measurement could not affect the analysis of Typhoon Kilo on the upstream side: Easterly winds were frequently observed by seabird soaring along the east coast of Tohoku Region.

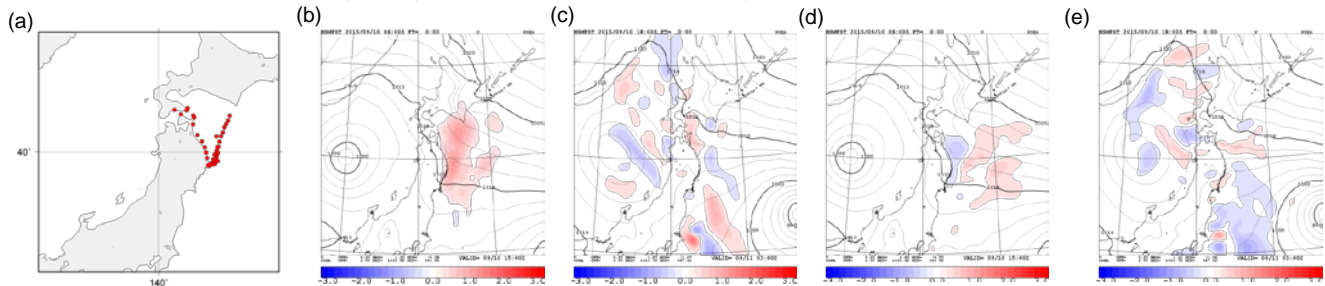


Figure 1 (a) Horizontal distribution of the locations of surface winds measurement during the observation period. (b) Horizontal distribution of the difference in surface zonal winds (color shades) between CTL and TEST (TEST-CTL) at 0600 UTC 10 September, (c) same as (b) except at 1800 UTC, (d) same as (b) except in the surface meridional winds and (e) same as (d) except at 1800 UTC with simulated sea-level pressures. The contour interval is 2 hPa.

### 3.2 Impacts for forecasts on local heavy rainfalls

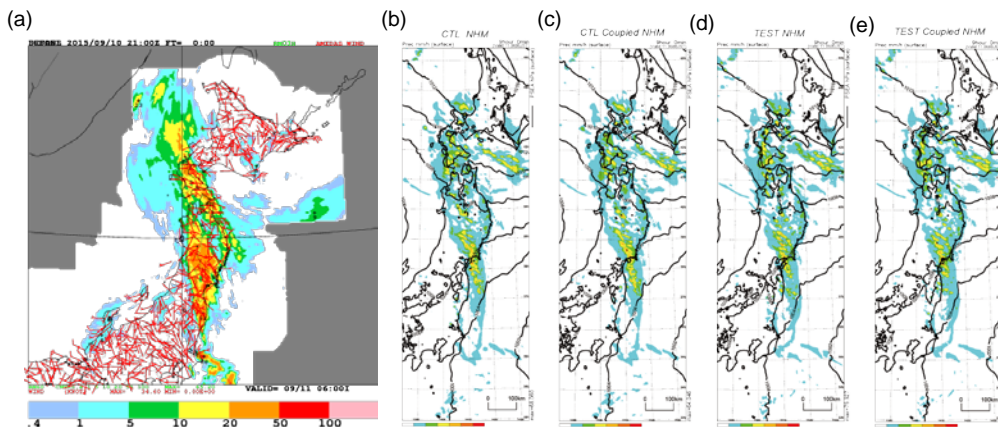


Figure 2 (a) Horizontal distribution of analyzed hourly rainfalls (shades) with 10-m winds (red vectors) at 1800UTC 10 September. (b-e) Horizontal distributions of hourly rainfall forecasts (b) by the NHM and (c) by the coupled NHM in the CTL experiment and (d) by the NHM and (e) by the coupled NHM in the TEST experiment. Contours indicate sea-level pressures with the interval of 2 hPa.

Figure 2a shows the horizontal distribution of analyzed hourly rainfall and 10-m winds at 1800 UTC 10 September. A linear rainband with two locally salient linearly rainfall areas was analyzed in the northern Japan Region, including Tohoku Region. Figures 2b-e show the results of numerical simulation for a 9-h forecast starting at 1200 UTC, valid 3 hours later than the analysis shown in Figure 2a. A linear rainband shown in Figure 2a was reasonably simulated at that time. There was no significant difference among the four experiments: simulations by the NHM and the coupled NHM in the CTL experiment and those in the TEST experiment. The results suggest that there was less impact on the linear rainfall of surface winds measurement by seabirds soaring over the ocean although the heavy precipitation occurred on the downstream side of the observations and the difference propagated toward the location of the linear rainband.

### 4. Concluding remarks

We set the horizontal resolution of 15 km and the assimilation interval of 1 hour in the TEST experiment, which seems to be too coarse to utilize in situ observations more efficiently because the area of the observations was spatially and temporally limited. Further computational resources are needed to conduct the assimilation experiments by high-resolution NHM-LETKF and to investigate the impact more precisely.

### Acknowledgements

This work was supported by JSPS KAKENHI Grant Number JP26800247 and JST CREST Grant Number JPMJCR1685, Japan.

### References

Kunii, M. (2014). Mesoscale data assimilation for a local severe rainfall event with the NHM-LETKF system. *Weather and Forecasting*, (2013). <http://dx.doi.org/10.1175/WAF-D-13-00032.1>.  
 Yonehara Y., Y. Goto, K. Yoda, Y. Watanuki, L. C. Young, H. Weimerskirch, C.-A. Bost and K. Sato (2016), Flight paths of seabirds soaring over the ocean surface enable measurement of fine-scale wind speed and direction. *PNAS* 113, 9039-9044. DOI: 10.1073/pnas.1523853113.  
 Wada, A., N. Kohno and Y. Kawai (2010). Impact of wave-ocean interaction on Typhoon Hai-Tang in 2005. *SOLA*, 6A, 13-16.  
 Whitaker, J. S., and T. M. Hamill (2012), Evaluating Methods to Account for System Errors in Ensemble Data Assimilation, *Mon. Weather Rev.*, 140, 3078–3089.

# Development of a Rapid-Update Real-Time Mesoscale Analysis of Ceiling and Visibility

Runhua Yang<sup>1,2</sup>, Manuel Pondeca<sup>1,2</sup>, Steven Levine<sup>2,3</sup>, Geoff DiMego<sup>2</sup>,  
Jeff Whiting<sup>1,2</sup>, Jacob Carley<sup>1,2</sup>, Geoff Manikin<sup>2</sup>, Annette Gibbs<sup>1,2</sup>

<sup>1</sup> I.M. Systems Group, Inc., <sup>2</sup> NOAA NWS/National Centers for Environmental, US

<sup>3</sup> Systems Research Group, Colorado Springs, CO

Email: [Runhua.Yang@noaa.gov](mailto:Runhua.Yang@noaa.gov)

## Objective and background

A Rapid-Update Real-Time Mesoscale Analysis (RU-RTMA) system is an extension of RTMA from an hourly analysis to a 15 minute analysis, which is developed primarily to provide a near-real time grid analysis of surface visibility and ceiling height for the Helicopter Emergency Medical Services (HEMS) tool running at the Aviation Weather Center, NOAA.

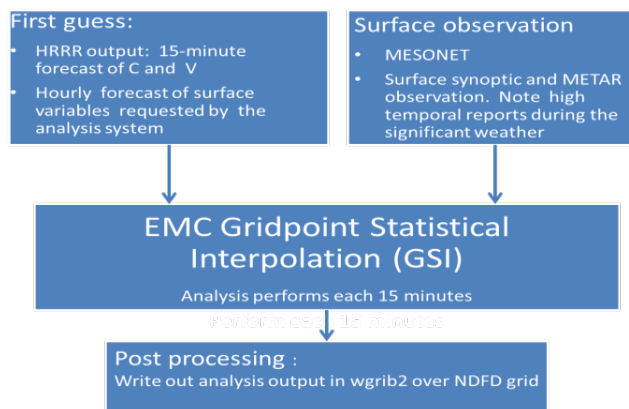
The full set of products comprise a gridded analysis of surface visibility and ceiling height (C and V), surface pressure, temperature and moisture at 2 meters, and wind speed and direction, as well as wind gust, all at 10m. The products are available for the contiguous United States (CONUS).

The following three aspects enable the development of RU-RTMA: (1) The advent of the HRRR, a high resolution numerical weather forecast model with a sophisticated cloud prediction scheme; (2) the existence of a reliable and dense network of observations; and (3) the prior development of the RTMA, which includes an hourly analysis of C and V. (Pondeca et al. 2016a, 2016b)

Considerable effort has been devoted to RU-RTMA's computing efficiency in order to deliver the analysis products no later than 20 minutes past the analysis time. With the emphasis on C and V, the observation selection algorithm of the original RTMA was modified to select only one observation per site, specifically, the one closest to the analysis time. Most C and V observations are from METAR sites, which are normally reported hourly. However, in the advent of affecting-flight weather systems, sub-hourly special reports (SPECIs) are also generated. Although SPECI reports are not particularly numerous, they are extremely important to RU-RTMA by reflecting the current weather conditions. The modified algorithm ensures the SPECIs always get the strongest weight in the analysis. The typical window of the observations ranges from 30 minutes before to 8 minutes after the analysis time.

## RU-RTMA system

RU-RTMA includes four components: preparation of the first guess for the analysis; preparation of the observation files; the analysis itself, which is performed with EMC's gridpoint statistical interpolation (GSI) system; and the post processing, which converts the analysis to GRIB2 format. Below is a schematic illustration of the RU-RTMA components.



## Preliminary Results

The quality of the RTMA depends on several aspects, including accuracy of the estimated forecast error covariance and observation error covariance. In particular, the known non-normal distribution of the observation innovations for C and V as well as the discrete nature of these parameters renders the analysis particularly challenging. Of note is that currently only static error statistics are used in RTMA. RU-RTMA faces similar challenges as the hourly RTMA. In addition, because of the small observation time window, fewer observations are included in the RU-RTMA assimilation than in RTMA, which has a dump window of roughly +/- 30 minutes around the center of each hour.

Our first overall check is to compare the number of observations read in and the observations assimilated between RU-RTMA and RTMA, as shown in the Table below for the selected analysis time of 0000Z 17 December 2016. The number of observations for each 15-min window is less than that in RTMA, but the sum is more than that in the RTMA, as expected. The behavior of RTMA and RU-RTMA is similar in the number of assimilated observations.

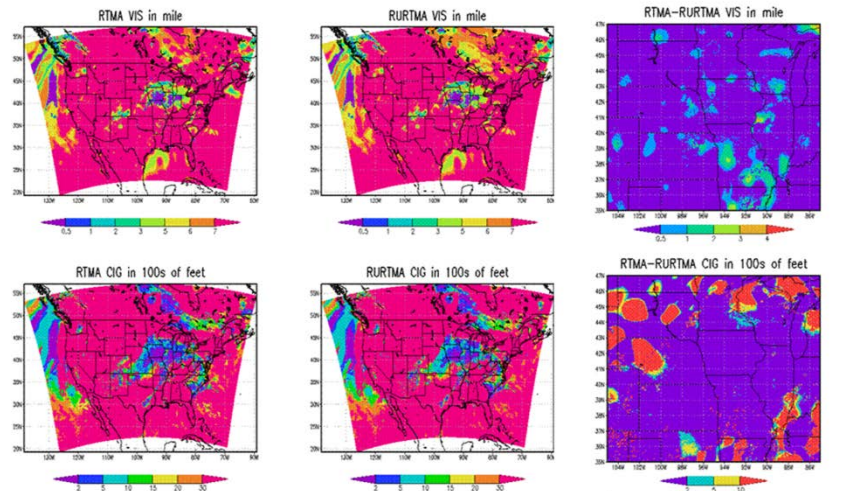
RU-RTMA: Total number of obs read in for each 15-min analysis (Top). Number of assimilated obs when only one ob per site is selected (bottom). VIS denotes visibility, CIG denotes ceiling height.

RTMA: Total number of obs read in within a one hour window (top). Number of obs assimilated (bottom). VIS denotes visibility, CIG denotes cloud

RURTMA	00min	15min	30min	45min	SUM
VIS	87356	104171	63212	60031	314770
CIG	83213	97509	57254	56424	294400
RURTMA	00min	15min	30min	45min	SUM
VIS	49534	53648	33508	30509	167199
CIG	42409	44882	28341	26849	142481

Hourly RTMA	One hour dump window @ 00min
VIS	280639
CIG	132122
Hourly RTMA	assimilated
VIS	102258
CIG	97777

Figure 1 Comparison of surface visibility (in miles, top panels) and ceiling height (in 100's of feet, bottom panels) between hourly RTMA (left column) and RU-RTMA (middle column) for 0000Z 17 Jan. 2017. The pattern and magnitude are quite similar. Note that both systems show a center of low C and V over the Midwest States. The third column shows the difference plot (RTMA minus Ru-RTMA) over this center. No significant differences are seen.



### On-going work

Continue to assess the quality of the initial 15-min C&V products for CONUS. Compute verification statistics using independent data. Extend RU-RTMA to Alaska.

For RU-RTMA data information, contact Runhua.Yang@noaa.gov or Steven.Levine@noaa.gov

### Reference

Pondeca et al. 2016a: Research Activities in Atmospheric and Oceanic Modeling (Blue Book).

Pondeca et al. 2016b: RTMA/URM v2.5.0

[https://docs.google.com/presentation/d/1NQt\\_FleS082uPwEzpZ7Ec4pEfi7s6Ly9F81CDM78GX0/edit#slide=id.p](https://docs.google.com/presentation/d/1NQt_FleS082uPwEzpZ7Ec4pEfi7s6Ly9F81CDM78GX0/edit#slide=id.p)

### Acknowledgements

We are grateful to Wesley Ebisuzaki at NOAA for providing his wgrib2 software.

The FAA Aviation Weather Research Program is acknowledged for their support of this project.